A high-order shock capturing discontinuous Galerkin–finite difference hybrid method for GRMHD

IOP Publishing Classical and Quantum Gravity
Class. Quantum Grav. **39** (2022) 195001 (41pp) https://doi.org/10.1088/1361-6382/ac8864

A high-order shock capturing discontinuous Galerkin–finite difference hybrid method for GRMHD

Nils Deppe[1,*], **François Hébert**[1], **Lawrence E Kidder**[2] and **Saul A Teukolsky**[1,2]

[1] Theoretical Astrophysics 350-17, California Institute of Technology, Pasadena, CA 91125, United States of America
[2] Cornell Center for Astrophysics and Planetary Science, Cornell University, Ithaca, NY 14853, United States of America

E-mail: ndeppe@caltech.edu

Received 22 April 2022, revised 30 July 2022
Accepted for publication 9 August 2022
Published 26 August 2022

Abstract

We present a discontinuous Galerkin (DG)–finite difference (FD) hybrid scheme that allows high-order shock capturing with the DG method for general relativistic magnetohydrodynamics. The hybrid method is conceptually quite simple. An unlimited DG candidate solution is computed for the next time step. If the candidate solution is inadmissible, the time step is retaken using robust FD methods. Because of its *a posteriori* nature, the hybrid scheme inherits the best properties of both methods. It is high-order with exponential convergence in smooth regions, while robustly handling discontinuities. We give a detailed description of how we transfer the solution between the DG and FD solvers, and the troubled-cell indicators necessary to robustly handle slow-moving discontinuities and simulate magnetized neutron stars. We demonstrate the efficacy of the proposed method using a suite of standard and very challenging 1D, 2D, and 3D relativistic magnetohydrodynamics test problems. The hybrid scheme is designed from the ground up to efficiently simulate astrophysical problems such as the inspiral, coalescence, and merger of two neutron stars.

Keywords: discontinuous Galerkin, finite difference, GRMHD, neutron star, WENO

(Some figures may appear in colour only in the online journal)

*Author to whom any correspondence should be addressed.

1. Introduction

The discontinuous Galerkin (DG) method was first presented by Reed and Hill [1] to solve the neutron transport equation. Later, in a series of seminal papers, Cockburn and Shu applied the DG method to nonlinear hyperbolic conservation laws [2–4]. A very important property of the DG method is that it guarantees linear stability in the L_2 norm for arbitrary high order, which was proven for the scalar case in [5] and for systems in [6, 7]. While this means the DG method is very robust, DG alone is still subject to Godunov's theorem [8]: at high order it produces oscillatory solutions. Accordingly, it requires some nonlinear supplemental method for stability in the presence of discontinuities and large gradients. A large number of different methods for limiting the DG solution to achieve such stability have been proposed. The basic idea shared by all the limiters is to detect troubled cells or elements (i.e., those whose solution is too oscillatory or has some other undesirable property), then apply some nonlinear reconstruction using the solution from neighboring elements. This idea is largely an extension of what has worked well for finite-volume (FV) and finite-difference (FD) shock-capturing methods.

In this paper we follow a different avenue that, to the best of our knowledge, was first proposed in [9]. The idea is to supplement a high-order spectral-type method—such as pseudospectral collocation or, in our case, DG—with robust FV or FD shock-capturing methods. If the solution in an element is troubled or inadmissible, the solution is projected to a FV or FD grid and evolved with existing robust shock-capturing methods. This approach has been applied to DG supplemented with FV in [10–16]. The major breakthrough in [12] was applying the shock detection and physical realizability checks on the solution *after* the time step is taken and redoing the step if the solution is found to be inadmissible. We follow this *a posteriori* approach because it allows us to guarantee a physically realizable solution (e.g., positive density and pressure), as well as allowing us to prevent unphysical oscillations from entering the numerical solution. This procedure is in strong contrast to classical limiting strategies, where effectively a filter is applied to the DG solution in an attempt to remove spurious oscillations.

High-order pseudospectral methods have proven extremely useful in producing a large number of long and accurate gravitational waveforms from binary black hole merger simulations [17–25] as well as other applications in relativistic astrophysics [26–31]. Since binary inspirals emit gravitational radiation, the numerical solution in most of the computational domain is smooth but non-constant, and so high-order methods are preferable. During the inspiral portion of a binary neutron star merger, the only discontinuities present are at the stellar surfaces. This suggests that high-order methods can be used in most of the computational domain. Specifically, the hydro solution inside the star is smooth, and while outside the star the hydro evolution is not necessary, the Einstein equations still need to be solved and have a smooth solution. The use of high-order methods allows for a significant reduction in computational cost of the simulation, which is especially important for reducing the computational cost of producing a large gravitational waveform catalog for binary neutron star mergers.

We present a detailed derivation and description of our DG–FD hybrid scheme and how we use it to solve the equations of general relativistic magnetohydrodynamics (GRMHD). To the best of our knowledge, the algorithm is the first to successfully evolve a 3D magnetized Tolman–Oppenheimer–Volkoff (TOV) star using DG methods. In section 2 we briefly review the equations of GRMHD. In section 3 we give a brief overview of DG and conservative FD methods, provide a new simple form of the moving mesh evolution equations, and discuss the time step size restrictions of the DG and FD methods. In section 4 we state our requirements

from a DG limiter or DG hybrid scheme, and then give an overview of common limiters currently used, including which of our requirements they meet. The new DG–FD hybrid scheme is described in section 5. Specifically, we discuss how to handle the intercell fluxes between elements using DG and FD, the idea of applying the troubled-cell indicators (TCIs) *a posteriori*, the TCIs we use, and a new perspective on how DG–FD hybrid schemes should be interpreted. In section 6 we present numerical results from the open-source code `SpECTRE` [32, 33] using our scheme and conclude in section 7.

2. Equations of GRMHD

We adopt the standard 3 + 1 form of the spacetime metric, (see, e.g., [34, 35]),

$$\mathrm{d}s^2 = g_{ab}\,\mathrm{d}x^a\mathrm{d}x^b = -\alpha^2\,\mathrm{d}t^2 + \gamma_{ij}\big(\mathrm{d}x^i + \beta^i\,\mathrm{d}t\big)\big(\mathrm{d}x^j + \beta^j\,\mathrm{d}t\big), \tag{1}$$

where α is the lapse, β^i the shift vector, and γ_{ij} is the spatial metric. We use the Einstein summation convention, summing over repeated indices. Latin indices from the first part of the alphabet $a, b, c, \ldots$ denote spacetime indices ranging from 0 to 3, while Latin indices $i, j, \ldots$ are purely spatial, ranging from 1 to 3. We work in units where $c = G = M_\odot = 1$.

`SpECTRE` currently solves equations in flux-balanced and first-order hyperbolic form. The general form of a flux-balanced conservation law in a curved spacetime is

$$\partial_t u + \partial_i F^i = S, \tag{2}$$

where u is the state vector, F^i are the components of the flux vector, and S is the source vector.

We refer the reader to the literature [34, 36, 37] for a detailed description of the equations of GRMHD. If we ignore self-gravity, the GRMHD equations constitute a closed system that may be solved on a given background metric. We denote the rest-mass density of the fluid by ρ and its four-velocity by u^a, where $u^a u_a = -1$. The dual of the Faraday tensor F^{ab} is

$${}^*F^{ab} = \frac{1}{2}\epsilon^{abcd}F_{cd}, \tag{3}$$

where ϵ^{abcd} is the Levi-Civita tensor. Note that the Levi-Civita tensor is defined here with the convention [38] that in flat spacetime $\epsilon_{0123} = +1$. The equations governing the evolution of the GRMHD system are:

$$\nabla_a(\rho u^a) = 0 \quad \text{(rest-mass conservation)}, \tag{4}$$

$$\nabla_a T^{ab} = 0 \quad \text{(energy–momentum conservation)}, \tag{5}$$

$$\nabla_a {}^*F^{ab} = 0 \quad \text{(homogeneous Maxwell equation)}. \tag{6}$$

In the ideal MHD limit the stress tensor takes the form

$$T^{ab} = (\rho h)^* u^a u^b + p^* g^{ab} - b^a b^b \tag{7}$$

where

$$b^a = -{}^*F^{ab}u_b \tag{8}$$

is the magnetic field measured in the comoving frame of the fluid, and $(\rho h)^* = \rho h + b^2$ and $p^* = p + b^2/2$ are the enthalpy density and fluid pressure augmented by contributions of magnetic pressure $p_{\mathrm{mag}} = b^2/2$, respectively.

We denote the unit normal vector to the spatial hypersurfaces as n^a, which is given by

$$n^a = \left(1/\alpha, -\beta^i/\alpha\right)^{\mathrm{T}}, \tag{9}$$

$$n_a = (-\alpha, 0, 0, 0). \tag{10}$$

The spatial velocity of the fluid as measured by an observer at rest in the spatial hypersurfaces ('Eulerian observer') is

$$v^i = \frac{1}{\alpha}\left(\frac{u^i}{u^0} + \beta^i\right), \tag{11}$$

with a corresponding Lorentz factor W given by

$$W = -u^a n_a = \alpha u^0 = \frac{1}{\sqrt{1 - \gamma_{ij} v^i v^j}} \tag{12}$$

$$= \sqrt{1 + \gamma^{ij} u_i u_j} = \sqrt{1 + \gamma^{ij} W^2 v_i v_j}. \tag{13}$$

The electric and magnetic fields as measured by an Eulerian observer are given by

$$E^i = F^{ia} n_a = \alpha F^{0i}, \tag{14}$$

$$B^i = -{}^*F^{ia} n_a = -\alpha {}^*F^{0i}. \tag{15}$$

Finally, the comoving magnetic field b^a in terms of B^i is

$$b^0 = \frac{W}{\alpha} B^i v_i, \tag{16}$$

$$b^i = \frac{B^i + \alpha b^0 u^i}{W}, \tag{17}$$

while $b^2 = b^a b_a$ is given by

$$b^2 = \frac{B^2}{W^2} + (B^i v_i)^2. \tag{18}$$

We now recast the GRMHD equations in a $3 + 1$ split by projecting them along and perpendicular to n^a [36]. One of the main complications when solving the GRMHD equations numerically is preserving the constraint

$$\partial_i(\sqrt{\gamma} B^i) = 0, \tag{19}$$

where $\gamma = \det(\gamma_{ij})$ is the determinant of the spatial metric. Analytically, initial data evolved using the dynamical Maxwell equations are guaranteed to preserve the constraint. However, numerical errors generate constraint violations that need to be controlled. We opt to use the generalized Lagrange multiplier or divergence cleaning method [39] where an additional field Φ is evolved in order to propagate constraint violations out of the domain. Our version is very close to the one in [40]. The augmented system can still be written in flux-balanced form, where

the conserved variables are

$$u = \sqrt{\gamma}\begin{pmatrix} D \\ S_i \\ \tau \\ B^i \\ \Phi \end{pmatrix} = \begin{pmatrix} \tilde{D} \\ \tilde{S}_i \\ \tilde{\tau} \\ \tilde{B}^i \\ \tilde{\Phi} \end{pmatrix}$$
$$= \sqrt{\gamma}\begin{pmatrix} \rho W \\ (\rho h)^* W^2 v_i - \alpha b^0 b_i \\ (\rho h)^* W^2 - p^* - \left(\alpha b^0\right)^2 - \rho W \\ B^i \\ \Phi \end{pmatrix}, \tag{20}$$

with corresponding fluxes

$$F^i = \begin{pmatrix} \tilde{D} v^i_{\rm tr} \\ \tilde{S}_j v^i_{\rm tr} + \alpha\sqrt{\gamma} p^* \delta^i_j - \alpha b_j \tilde{B}^i / W \\ \tilde{\tau} v^i_{\rm tr} + \alpha\sqrt{\gamma} p^* v^i - \alpha^2 b^0 \tilde{B}^i / W \\ \tilde{B}^j v^i_{\rm tr} - \alpha v^j \tilde{B}^i + \alpha \gamma^{ij} \tilde{\Phi} \\ \alpha \tilde{B}^i - \tilde{\Phi}\beta^i \end{pmatrix}, \tag{21}$$

and corresponding sources

$$S = \begin{pmatrix} 0 \\ (\alpha/2)\tilde{S}^{kl}\partial_i \gamma_{kl} + \tilde{S}_k \partial_i \beta^k - \tilde{E}\partial_i \alpha \\ \alpha \tilde{S}^{kl} K_{kl} - \tilde{S}^k \partial_k \alpha \\ -\tilde{B}^j \partial_j \beta^i + \Phi \partial_k (\alpha\sqrt{\gamma}\gamma^{ik}) \\ \alpha \tilde{B}^k \partial_k \ln \alpha - \alpha K \tilde{\Phi} - \alpha\kappa\tilde{\Phi} \end{pmatrix}. \tag{22}$$

The transport velocity is defined as $v^i_{\rm tr} = \alpha v^i - \beta^i$ and the generalized energy $\tilde{E}$ and source $\tilde{S}^{ij}$ are given by

$$\tilde{E} = \tilde{\tau} + \tilde{D}, \tag{23}$$

$$\tilde{S}^{ij} = \sqrt{\gamma}\left[(\rho h)^* W^2 v^i v^j + p^* \gamma^{ij} - \gamma^{ik}\gamma^{jl} b_k b_l\right]. \tag{24}$$

3. The DG and conservative FD methods

We are interested in solving nonlinear hyperbolic conservation laws of the form

$$\partial_a F^a = \partial_t u + \partial_i F^i = S, \tag{25}$$

where u are the evolved/conserved variables, F^i are the fluxes, and S are the source terms.

3.1. DG method

In the DG method the computational domain is divided up into non-overlapping elements or cells, which we denote by Ω_k. This allows us to write the conservation law (25) as a semi-discrete system, where time remains continuous. In the DG method one integrates the evolution equation (25) against spatial basis functions of degree N, which we denote by $\phi_{\tilde{i}}$. We index the

basis functions and collocation points of the DG scheme with breve Latin indices, e.g. $\breve{\imath}, \breve{\jmath}, \breve{k}$. The basis functions are defined in the reference coordinates of each element, which we denote by $\xi^{\hat{\imath}}$. We use hatted indices to denote tensor components in the reference frame. The reference coordinates are mapped to the physical coordinates using the general function

$$x^i = x^i(\xi^{\hat{\imath}}). \tag{26}$$

We will discuss making the mapping time-dependent in section 3.3 below.

In the DG method we integrate the basis functions against (25),

$$\int_{\Omega_k} \mathrm{d}^3x\, \phi_{\breve{\imath}} \left[\partial_t u + \partial_i F^i - S\right] = 0, \tag{27}$$

where repeated indices are implicitly summed over. Note that we are integrating over the physical coordinates, not the reference coordinates $\xi^{\hat{\imath}}$. Following the standard prescription where we integrate by parts and replace the flux on the boundary $n_i F^i$ with a boundary term G (a numerical flux dotted into the normal to the surface), we obtain the weak form

$$\int_{\Omega_k} \mathrm{d}^3x\, \phi_{\breve{\imath}} [\partial_t u - S] - \int_{\Omega_k} \mathrm{d}^3x\, F^i \partial_i \phi_{\breve{\imath}} + \oint_{\partial\Omega_k} \mathrm{d}^2\Sigma\, \phi_{\breve{\imath}} G = 0, \tag{28}$$

where $\partial\Omega_k$ is the boundary of the element and $\mathrm{d}^2\Sigma$ is the surface element. Undoing the integration by parts gives us the equivalent strong form

$$\int_{\Omega_k} \mathrm{d}^3x\, \phi_{\breve{\imath}} \left[\partial_t u + \partial_i F^i - S\right] + \oint_{\partial\Omega_k} \mathrm{d}^2\Sigma\, \phi_{\breve{\imath}} \left(G - n_i F^i\right) = 0, \tag{29}$$

where n_i is the outward-pointing unit normal covector in the physical frame. Next, we use a nodal DG method and expand the various terms using the basis $\phi_{\breve{\imath}}$ as

$$u = \sum_{\breve{\imath}=0}^{N} u_{\breve{\imath}} \phi_{\breve{\imath}}. \tag{30}$$

The weak form can be written as

$$\int_{\Omega_k} \mathrm{d}^3x\, \phi_{\breve{\imath}} \phi_{\breve{k}} \left[\partial_t u_{\breve{k}} - S_{\breve{k}}\right] - \int_{\Omega_k} \mathrm{d}^3x\, F^i_{\breve{k}} \phi_{\breve{k}} \partial_i \phi_{\breve{\imath}} + \oint_{\partial\Omega_k} \mathrm{d}^2\Sigma\, \phi_{\breve{\imath}} \phi_{\breve{k}} G_{\breve{k}} = 0. \tag{31}$$

The equivalent strong form is

$$\int_{\Omega_k} \mathrm{d}^3x\, \phi_{\breve{\imath}} \phi_{\breve{k}} \left[\partial_t u_{\breve{k}} + (\partial_i F^i)_{\breve{k}} - S_{\breve{k}}\right] + \oint_{\partial\Omega_k} \mathrm{d}^2\Sigma\, \phi_{\breve{\imath}} \phi_{\breve{k}} \left(G - n_i F^i\right)_{\breve{k}} = 0. \tag{32}$$

In the strong form we have expanded $\partial_i F^i$ in the basis, which might lead to aliasing [41]. In practice, we have not encountered any aliasing-driven instabilities that require filtering.

In order to simplify the scheme, we use a tensor-product basis of 1D Lagrange interpolating polynomials with Legendre–Gauss–Lobatto collocation points. We denote this DG scheme with 1D basis functions of degree N by P_N. A P_N scheme is expected to converge at order $\mathcal{O}(\Delta x^{N+1})$ for smooth solutions [42], where Δx is the 1D size of the element. The reference elements are intervals in 1D, squares in 2D, and cubes in 3D, where each component of the reference coordinates $\xi^{\hat{\imath}} \in [-1, 1]$. We use the map $x^i(\xi^{\hat{\imath}})$ to deform the squares and cubes into different shapes needed to produce an efficient covering of the domain. For example, if spherical geometries are present, we use $x^i(\xi^{\hat{\imath}})$ to create a cubed-sphere domain.

3.2. Conservative FD methods

Conservative FD methods evolve the cell-center values, but the cell-face values (the midpoints along each axis) are necessary for solving the Riemann problem and computing the FD derivatives of the fluxes. Denoting the numerical flux by $\hat{F}^i$ and the kth-order FD derivative operator by $D^{(k)}_{\hat{i}}$, we can write the semi-discrete evolution equations as

$$\partial_t u_{\underline{i}} + \left(\frac{\partial \xi^{\hat{i}}}{\partial x^i}\right)_{\underline{i}} \left(D^{(k)}_{\hat{i}} \hat{F}^i\right)_{\underline{i}} = S_{\underline{i}}, \tag{33}$$

where we use underlined indices to label FD cells/grid points. Equation (33) can be rewritten to more closely resemble the DG form since we actually use G as the numerical flux $\hat{F}^i$ on the cell boundary. Specifically,

$$\partial_t u_{\underline{i}} + \frac{1}{J_{\underline{i}}} \sum_{\hat{i}} \left[D^{(k)}_{\hat{i}} \left(J \sqrt{\frac{\partial \xi^{\hat{i}}}{\partial x^i} \gamma^{ij} \frac{\partial \xi^{\hat{i}}}{\partial x^j}} G^{(\hat{i})} \right) \right]_{\underline{i}} = S_{\underline{i}}, \tag{34}$$

where J is the determinant of the Jacobian matrix $\partial x^i / \partial \xi^{\hat{i}}$. This form allows our implementation to reuse as much of the DG Riemann solvers as possible, and also makes interfacing between the DG and FD methods easier. Ultimately, we use a flux-difference-splitting scheme, where we reconstruct the primitive variables to the interfaces between cells. Which reconstruction method we use is stated for each test problem below.

3.3. Moving mesh formulation

Moving the mesh to follow interesting features of the solution can greatly reduce computational cost. A moving mesh is also essential for evolutions of binary black holes, one of our target applications, where the interior of the black holes needs to be excised to avoid the singularities [23, 43]. Here we present a new form of the moving mesh evolution equations that is extremely simple to implement and derive. We assume that the velocity of the mesh is some spatially smooth function, though this assumption can be removed if one uses the path-conservative methods described in [44] based on Dal Maso–LeFloch–Murat theory [45]. We write the map from the reference coordinates to the physical coordinates as

$$t = \hat{t}, \quad x^i = x^i(\xi^{\hat{i}}, \hat{t}). \tag{35}$$

The spacetime Jacobian matrix is given by

$$\frac{\partial x^a}{\partial \xi^{\hat{a}}} = \begin{pmatrix} \dfrac{\partial t}{\partial \hat{t}} & \dfrac{\partial t}{\partial \xi^{\hat{i}}} \\ \dfrac{\partial x^i}{\partial \hat{t}} & \dfrac{\partial x^i}{\partial \xi^{\hat{i}}} \end{pmatrix} = \begin{pmatrix} 1 & 0 \\ v^i_g & \dfrac{\partial x^i}{\partial \xi^{\hat{i}}} \end{pmatrix}, \tag{36}$$

where the mesh velocity of the physical frame is defined as

$$v^i_g = \frac{\partial x^i}{\partial \hat{t}}. \tag{37}$$

The inverse spacetime Jacobian matrix is given by

$$\frac{\partial \xi^{\hat{a}}}{\partial x^a} = \begin{pmatrix} \dfrac{\partial \hat{t}}{\partial t} & \dfrac{\partial \hat{t}}{\partial x^i} \\ \dfrac{\partial \xi^{\hat{i}}}{\partial t} & \dfrac{\partial \xi^{\hat{i}}}{\partial x^i} \end{pmatrix} = \begin{pmatrix} 1 & 0 \\ v^{\hat{i}}_g & \left(\dfrac{\partial x^i}{\partial \xi^{\hat{i}}}\right)^{-1} \end{pmatrix}, \tag{38}$$

where the mesh velocity in the reference frame is given by

$$v_g^{\hat{i}} \equiv \frac{\partial \xi^{\hat{i}}}{\partial t} = -\frac{\partial \xi^{\hat{i}}}{\partial x^i} v_g^i. \tag{39}$$

When composing coordinate maps the velocities combine as:

$$v_g^i = \frac{\partial x^i}{\partial \hat{t}} = \frac{\partial x^i}{\partial \tilde{t}} + \frac{\partial x^i}{\partial X^{\tilde{i}}} \frac{\partial X^{\tilde{i}}}{\partial \hat{t}}, \tag{40}$$

where a new intermediate frame with coordinates $\{\tilde{t}, X^{\tilde{i}}\}$ is defined and $X^{\tilde{i}} = X^{\tilde{i}}\left(\xi^{\hat{i}}, \hat{t}\right)$.

To obtain the moving mesh evolution equations, we need to transform the time derivative in (25) from being with respect to t to being with respect to $\hat{t}$. Starting with the chain rule for $\partial u/\partial \hat{t}$, we get

$$\frac{\partial u}{\partial t} = \frac{\partial u}{\partial \hat{t}} - \frac{\partial x^i}{\partial \hat{t}} \partial_i u = \partial_i u - \partial_i\left(v_g^i u\right) + u \partial_i v_g^i. \tag{41}$$

Substituting (41) into (25) we get

$$\partial_t u + \partial_i\left(F^i - v_g^i u\right) = S - u \partial_i v_g^i. \tag{42}$$

This formulation of the moving mesh equations is simpler than the common arbitrary Lagrangian–Eulerian formulation [46].

The same DG or FD scheme used to discretize (25) can be used to discretize (42). In the case that v_g^i is an evolved variable, the additional term should be treated as a nonconservative product using the path-conservative formalism [44]. Finally, we note that the characteristic fields are unchanged by the mesh movement, but the characteristic speeds λ are changed to $\lambda \to \lambda - n_i v_g^i$.

3.4. Time discretization

We evolve the semi-discrete system (be it the DG or FD discretized system) in time using a method of lines. We use either a third-order strong-stability preserving Runge–Kutta method [47] or a forward self-starting Adams–Bashforth time stepper [48, 49]. Which method is used will be noted for each test case.

The DG method has a rather restrictive Courant–Friedrichs–Lewy (CFL) condition that decreases as the polynomial degree N of the basis is increased. The CFL number scales roughly as $1/(2N+1)$ [50, 51], which can be understood as a growth in the spectrum of the spatial discretization operator [52]. For a DG discretization in d spatial dimensions, the time step Δt must satisfy

$$\Delta t \leqslant \frac{1}{d(2N+1)} \frac{h}{|\lambda_{\max}|}, \tag{43}$$

where h is the characteristic size of the element and $\lambda_{\max}$ is the maximum characteristic speed of the system being evolved. For comparison, FV and FD schemes have a time step restriction of

$$\Delta t \leqslant \frac{1}{d} \frac{h}{|\lambda_{\max}|}, \tag{44}$$

where h is the characteristic size of the FV or FD cell. However, a DG element has $N+1$ grid points per dimension, while FV or FD cells only have one, and so the CFL condition for DG is partly offset by the increase in order that the algorithm provides.

4. Limiting in the DG method

In this section we give an overview of what we require from a DG limiter, followed by a brief discussion of existing limiters in the literature and which of our requirements they meet.

4.1. Requirements

We have several requirements that, when combined, are very stringent. However, we view these as necessary for DG to live up to the promise of a high-order shock-capturing method. In no particular order, we require that

Requirements 4.1

(a) Smooth solutions are resolved, i.e., smooth extrema are not flattened,
(b) Unphysical oscillations are removed,
(c) Physical realizability of the solution is guaranteed,
(d) Sub-cell or sub-element resolution is possible, i.e., discontinuities are resolved inside the element, not just at boundaries,
(e) Curved hexahedral elements are supported,
(f) Slow-moving shocks are resolved,
(g) Moving meshes are supported,
(h) Higher than fourth-order DG can be used.

Requirement 4.1(d) is necessary to justify the restrictive time step size, (43). That is, if discontinuities are only resolved at the boundaries of elements, the DG scheme results in excessive smearing. In such a scenario it becomes difficult to argue for using DG over FV or FD methods. While in principle it is possible to use adaptive mesh refinement or hp-adaptivity to switch to low-order DG at discontinuities, effectively switching to a low-order FV method, we are unaware of implementations that are capable of doing so for high-order DG.

We note that achieving higher-than-fourth order is especially challenging with many of the existing limiters. Since FV and FD methods of fourth or higher order are becoming more common, we view high order as being crucial for DG to be competitive with existing FV and FD methods, especially given the restrictive time step size.

4.2. Overview of existing DG limiters

Aside from the FV subcell limiters [10–12], DG limiters operate on the solution after a time step or substep is taken so as to remove spurious oscillations and sometimes also to correct unphysical values. This is generally achieved by some nonlinear reconstruction using the solution in neighboring elements. How exactly this reconstruction is done depends on the specific limiters, but all limiters involve two general steps:

(a) Detecting whether or not the solution in the element is 'bad' (TCIs),
(b) Correcting the degrees of freedom/solution in the element.

A good TCI avoids triggering the limiter where the solution is smooth while still preventing spurious unphysical oscillations. Unfortunately, making this statement mathematically rigorous is challenging and the last word is yet to be written on which TCIs are the best. Since the TCI may trigger in smooth regions, ideally the limiting procedure does not flatten local extrema when applied in such regions. In a companion paper [53] we have experimented with the (admittedly quite dated but very robust) minmod family of limiters [3, 4, 54], the hierarchical limiter of Krivodonova [55, 56], the simple WENO limiter [57], and the Hermite

WENO (HWENO) limiter [58]. While this does not include every limiter applicable to structured meshes, it covers the common ones. We will discuss each limiter in turn, reporting what we have found to be good and bad.

The minmod family of limiters [3, 4, 54] linearize the solution and decrease the slope if the slope is deemed to be too large. This means that the minmod limiters quickly flatten local extrema in smooth regions, do not provide sub-element resolution, and are not higher-than-fourth order. While they are extremely robust and tend to do a good job of maintaining physical realizability of the solution despite not guaranteeing it, the minmod limiters are simply too aggressive and low-order to make DG an attractive replacement for shock-capturing FD methods. Furthermore, generalizing the minmod limiters to curved elements in the naïve manner makes them very quickly destroy any symmetries of the domain decomposition and solution. Overall, we find that the minmod limiters satisfy only requirements 4.1(b), (f), and (g).

The hierarchical limiter of Krivodonova [55, 56] works by limiting the coefficients of the solution's modal representation, starting with the highest coefficient then decreasing in order until no more limiting is necessary. We find that in 1D the Krivodonova limiter works quite well, even using fourth-order elements. However, in 2D and 3D and for increasingly complex physical systems, the limiter fails. Furthermore, it is nontrivial to extend to curved elements since comparing modal coefficients assumes the Jacobian matrix of the map $x^i(\xi^{\hat{i}})$ is spatially uniform. The Krivodonova limiter satisfies requirements 4.1(a), (f), and (g). We find that how well the Krivodonova limiter works at removing unphysical oscillations depends on the physical system being studied.

The simple WENO [57] and the HWENO [58] limiters are quite similar to each other. When limiting is needed, these limiters combine the element's solution with a set of solution estimates obtained from the neighboring elements' solutions. An oscillation indicator is applied on each solution estimate to determine the convex nonlinear weights for the reconstruction. Overall, the WENO limiters are, by design, very similar to WENO reconstruction used in FV and FD methods. We have found that the WENO limiters are generally robust for second- and third-order DG, but start producing unphysical solutions at higher orders. The WENO limiters satisfy our requirements 4.1(a), (b), (f), and (g). When supplemented with a positivity-preserving limiter [59], the WENO schemes are also able to satisfy requirement 4.1(c).

In short, none of the above limiters satisfy even half of our requirements 4.1. Furthermore, they all have parameters that need to be tuned for them to work well on different problems. This is unacceptable in realistic astrophysics simulations, where a large variety of complex fluid interactions are occurring simultaneously in different parts of the computational domain, and it is impossible to tune parameters such that all fluid interactions are resolved.

The subcell limiters [10–12] are much more promising and we will extend them to meet *all* the requirements 4.1. We will focus on the scheme proposed in [12] since it satisfies most of requirements 4.1. The basic idea behind the DG-subcell scheme is to switch to FV or, as proposed here, FD if the high-order DG solution is inadmissible, either because of excessive oscillations or violation of physical requirements on the solution. This idea was first presented in [9], where a spectral scheme was hybridized with a WENO scheme. In [10, 11] the decision whether to switch to a FV scheme is made before a time step is taken. In contrast, the scheme presented in [12] undoes the time step (or substep if using a Runge–Kutta substep method) and switches to a FV scheme. The advantage of undoing the time (sub) step is that physical realizability of the solution can be guaranteed as long as the FV or FD scheme guarantees physical realizability. The scheme of [12] is often referred to as an *a posteriori* limiting approach, where the time step is redone using the more robust method. Given a TCI that does not allow

unphysical oscillations and a high-order positivity-preserving FV/FD method, the subcell limiters as presented in the literature meet all requirements except 4.1(e) (curved hexahedral elements), (f) (slow-moving shocks), and (g) (moving mesh), limitations that we will address below. The key feature that makes the DG-subcell scheme a very promising candidate for a generic, robust, and high-order method is that the limiting is not based on polynomial behavior alone but considers the *physics of the problem*. By switching to a low-order method to guarantee physical realizability, the DG-subcell scheme guarantees that the resulting numerical solution satisfies the governing equations, even if only at a low order locally in space and time. Moreover, the DG-subcell scheme can guarantee that unphysical solutions such as negative densities never appear.

5. DG–FD hybrid method

In this section we present our DG–FD hybrid scheme. The method is designed specifically to address *all* requirements 4.1, and means in particular that the method is a robust high-order shock-capturing method. We first discuss how to switch between the DG and FD grids. Then we explain how neighboring elements communicate flux information if one element is using DG while the other is using FD. Next we review the *a posteriori* idea and discuss the TCIs we use, when we apply them, and how we handle communication between elements. Finally, we discuss the number of subcells to use and provide a new perspective on the DG–FD hybrid scheme that makes the attractiveness of such a scheme clear. In appendix A we provide an example of how curved hexahedral elements can be handled.

5.1. Projection and reconstruction between DG and FD grids

We will denote the solution on the DG grid by $u_{\bar{i}}$ and the solution on the FD grid by $u_{\underline{i}}$. We need to determine how to project the solution from the DG grid to the FD grid and how to reconstruct the DG solution from the FD solution. For simplicity, we assume an isotropic number of DG collocation points $(N+1)^d$ and FD cells $(N_s)^d$. Since FD schemes evolve the solution value at the cell-center, one method of projecting the DG solution to the FD grid is to use interpolation. However, interpolation is not conservative and so we opt for an L_2 projection, which is conservative if projecting to a grid with equal or more degrees of freedom. That is, we assume that $N_s \geqslant N+1$. The L_2 projection minimizes the integral

$$\int_{-1}^{1} (u - \underline{u})^2 \,\mathrm{d}x = \int_{-1}^{1} (u - \underline{u})^2 J \,\mathrm{d}\xi \tag{45}$$

with respect to $\underline{u}$, where $\underline{u}$ is the solution on the FD subcells. While we derive the projection matrix in 1D, generalizing to 2D and 3D is straightforward for our tensor product basis. Substituting the nodal basis expansion into (45) we obtain

$$\int_{-1}^{1} \left[u_{\bar{i}} \ell_{\bar{i}}(\xi) u_{\bar{j}} \ell_{\bar{j}}(\xi) + u_{\underline{i}} \ell_{\underline{i}}(\xi) u_{\underline{j}} \ell_{\underline{j}}(\xi) - 2 u_{\underline{i}} \ell_{\underline{i}}(\xi) u_{\bar{i}} \ell_{\bar{i}}(\xi) \right] J \,\mathrm{d}\xi, \tag{46}$$

where $\ell_{\underline{j}}(\xi)$ are the Lagrange interpolating polynomials on the subcells (i.e. $\ell_{\underline{j}}(\xi_{\underline{i}}) = \delta_{\underline{j}\underline{i}}$). Varying (46) with respect to the coefficients $u_{\underline{i}}$ and setting the result equal to zero we get

$$\int_{-1}^{1} \left[u_{\underline{j}} \ell_{\underline{i}}(\xi) \ell_{\underline{j}}(\xi) - u_{\bar{i}} \ell_{\underline{i}}(\xi) \ell_{\bar{i}}(\xi) \right] \delta u_{\underline{i}} J \,\mathrm{d}\xi = 0. \tag{47}$$

Since (47) must be true for all variations $\delta u_{\underline{i}}$ we see that

$$\int_{-1}^{1}\left[u_{\underline{j}}\ell_{\underline{i}}(\xi)\ell_{\underline{j}}(\xi)-u_{\check{\imath}}\ell_{\underline{i}}(\xi)\ell_{\check{\imath}}(\xi)\right]J\,\mathrm{d}\xi=0. \tag{48}$$

By expanding the determinant of the Jacobian on the basis we can simplify (48) to get

$$u_{\underline{i}}J_{\underline{i}}\int_{-1}^{1}\ell_{\underline{i}}(\xi)\ell_{\underline{j}}(\xi)\,\mathrm{d}\xi=u_{\check{\imath}}J_{\check{\imath}}\int_{-1}^{1}\ell_{\check{\imath}}(\xi)\ell_{\underline{j}}(\xi)\,\mathrm{d}\xi. \tag{49}$$

Note that expanding uJ on the basis instead of u creates some decrease in accuracy and can cause aliasing if uJ is not fully resolved by the basis functions. However, this procedure allows us to cache the projection matrices to make the method more efficient. Furthermore, expanding the Jacobian on the basis means interpolation and projection are equal when $N_s \geqslant N+1$. We solve for $u_{\underline{i}}J_{\underline{i}}$ in (49) by inverting the matrix $\int_{-1}^{1}\ell_{\underline{i}}(\xi)\ell_{\underline{j}}(\xi)\,\mathrm{d}\xi$ and find that

$$\begin{aligned}u_{\underline{i}}J_{\underline{i}}&=\left(\int_{-1}^{1}\ell_{\underline{i}}(\xi)\ell_{\underline{j}}(\xi)\,\mathrm{d}\xi\right)^{-1}\int_{-1}^{1}\ell_{\check{\imath}}(\xi)\ell_{\underline{j}}(\xi)\,\mathrm{d}\xi u_{\check{\imath}}J_{\check{\imath}}\\&=\ell_{\check{\imath}}(\xi_{\underline{i}})u_{\check{\imath}}J_{\check{\imath}}=\mathcal{P}_{\underline{i}\check{\imath}}u_{\check{\imath}}J_{\check{\imath}},\end{aligned} \tag{50}$$

where $\mathcal{P}_{\underline{i}\check{\imath}}$ is the L_2 projection matrix.

Reconstructing the DG solution from the FD solution is a bit more involved. Denoting the projection operator by $\mathcal{P}$ and the reconstruction operator by $\mathcal{R}$, we desire the property

$$\mathcal{R}(\mathcal{P}(u_{\check{\imath}}J_{\check{\imath}}))=u_{\check{\imath}}J_{\check{\imath}}. \tag{51}$$

We also require that the integral of the conserved variables over the subcells is equal to the integral over the DG element. That is,

$$\int_{\Omega}u\,\mathrm{d}^3x=\int_{\Omega}\underline{u}\,\mathrm{d}^3x\implies\int_{\Omega}uJ\,\mathrm{d}^3\xi=\int_{\Omega}\underline{u}J\,\mathrm{d}^3\xi. \tag{52}$$

Since $N_s \geqslant N+1$ we need to solve a constrained linear least squares problem.

We will denote the weights used to numerically evaluate the integral over the subcells by $R_{\underline{i}}$ and the weights for the integral over the DG element by w_l. To find the reconstruction operator we need to solve the system

$$\sum_{\check{\imath}}\mathcal{P}_{\underline{i}\check{\imath}}u_{\check{\imath}}J_{\check{\imath}}=u_{\underline{i}}J_{\underline{i}}, \tag{53}$$

subject to the constraint

$$\sum_{\check{\imath}}w_{\check{\imath}}u_{\check{\imath}}J_{\check{\imath}}=\sum_{\underline{i}}R_{\underline{i}}u_{\underline{i}}J_{\underline{i}}. \tag{54}$$

We do so by using the method of Lagrange multipliers. Denoting the Lagrange multiplier by λ, we must minimize the functional

$$f=\left(\mathcal{P}_{\underline{i}\check{\imath}}u_{\check{\imath}}J_{\check{\imath}}-u_{\underline{i}}J_{\underline{i}}\right)\left(\mathcal{P}_{\underline{i}\check{\jmath}}u_{\check{\jmath}}J_{\check{\jmath}}-u_{\underline{i}}J_{\underline{i}}\right)-\lambda\left(w_{\check{\imath}}u_{\check{\imath}}J_{\check{\imath}}-R_{\underline{i}}u_{\underline{i}}J_{\underline{i}}\right) \tag{55}$$

with respect to $u_{\check{\imath}}J_{\check{\imath}}$ and λ. Doing so we obtain the Euler–Lagrange equations

$$\begin{pmatrix} 2\mathcal{P}_{\underline{i}\check{\imath}}\mathcal{P}_{\underline{i}\check{\jmath}} & -w_{\check{\imath}} \\ w_{\check{\imath}}\delta_{\check{\imath}\check{\jmath}} & 0 \end{pmatrix} \begin{pmatrix} u_{\check{\jmath}}J_{\check{\jmath}} \\ \lambda \end{pmatrix} = \begin{pmatrix} 2\mathcal{P}_{\underline{i}\check{\imath}} \\ R_{\underline{i}} \end{pmatrix} (u_{\underline{i}}J_{\underline{i}}). \tag{56}$$

Inverting the matrix on the left side of (56), we obtain

$$\begin{pmatrix} u_{\check{\jmath}}J_{\check{\jmath}} \\ \lambda \end{pmatrix} = \begin{pmatrix} 2\mathcal{P}_{\underline{i}\check{\imath}}\mathcal{P}_{\underline{i}\check{\jmath}} & -w_{\check{\imath}} \\ w_{\check{\imath}}\delta_{\check{\imath}\check{\jmath}} & 0 \end{pmatrix}^{-1} \begin{pmatrix} 2\mathcal{P}_{\underline{i}\check{\imath}} \\ R_{\underline{i}} \end{pmatrix} (u_{\underline{i}}J_{\underline{i}}). \tag{57}$$

To make the notation less cumbersome we suppress indices by writing $w_{\check{\imath}}$ as $\vec{w}$ and $w_{\check{\imath}}\delta_{\check{\imath}\check{\jmath}}$ as $\mathbf{w}$. Treating the matrix as a partitioned matrix, we invert it to find

$$\begin{pmatrix} 2\mathcal{P}\mathcal{P} & -\vec{w} \\ \mathbf{w} & 0 \end{pmatrix}^{-1} = \begin{pmatrix} \Pi - \Pi\vec{w}\mathcal{W}\mathbf{w}\Pi & \Pi\vec{w}\mathcal{W} \\ -\mathcal{W}\mathbf{w}\Pi & \mathcal{W} \end{pmatrix}. \tag{58}$$

Here we have defined

$$\Pi = (2\mathcal{P}\mathcal{P})^{-1}, \qquad \mathcal{W} = \left[\mathbf{w}(2\mathcal{P}\mathcal{P})^{-1}\vec{w}\right]^{-1}. \tag{59}$$

Substituting (58) into (57) and performing the matrix multiplication we get

$$\begin{pmatrix} u_{\check{\jmath}}J_{\check{\jmath}} \\ \lambda \end{pmatrix} = \begin{pmatrix} \Pi 2\mathcal{P} - \Pi\vec{w}\mathcal{W}\mathbf{w}\Pi 2\mathcal{P} + \Pi\vec{w}\mathcal{W}\vec{R} \\ -\mathcal{W}\mathbf{w}\Pi 2\mathcal{P} + \mathcal{W}\vec{R} \end{pmatrix}_{\check{\jmath}\underline{i}} u_{\underline{i}}J_{\underline{i}}, \tag{60}$$

where $\vec{R}$ is short for $R_{\underline{i}}$. We can see that the first row of (60) gives

$$u_{\check{\jmath}}J_{\check{\jmath}} = \left\{\Pi 2\mathcal{P} - \Pi\vec{w}\mathcal{W}\mathbf{w}\Pi 2\mathcal{P} + \Pi\vec{w}\mathcal{W}\vec{R}\right\}_{\check{\jmath}\underline{i}} u_{\underline{i}}J_{\underline{i}}, \tag{61}$$

and so the reconstruction matrix used to obtain the DG solution from the FD solution is given by

$$R_{\check{\jmath}\underline{i}} = \left\{\Pi 2\mathcal{P} - \Pi\vec{w}\mathcal{W}\mathbf{w}\Pi 2\mathcal{P} + \Pi\vec{w}\mathcal{W}\vec{R}\right\}_{\check{\jmath}\underline{i}}. \tag{62}$$

To show that the reconstruction matrix (62) satisfies (51) we start by substituting (62) into (51):

$$\begin{aligned} \mathcal{R}\mathcal{P}uJ &= \left\{\Pi 2\mathcal{P} - \Pi\vec{w}\mathcal{W}\mathbf{w}\Pi 2\mathcal{P} + \Pi\vec{w}\mathcal{W}\vec{R}\right\}\mathcal{P}uJ \\ &= \left\{\mathbb{1} - \Pi\vec{w}\mathcal{W}\mathbf{w} + \Pi\vec{w}\mathcal{W}\vec{R}\mathcal{P}\right\}uJ \\ &= \{\mathbb{1} - \Pi\vec{w}\mathcal{W}\mathbf{w} + \Pi\vec{w}\mathcal{W}\mathbf{w}\}uJ \\ &= uJ, \end{aligned} \tag{63}$$

where we used the constraint $\mathbf{w}uJ = \vec{R}\mathcal{P}uJ$. Thus, the matrix given in (62) is the reconstruction matrix for obtaining the DG solution from the FD solution on the subcells and is the pseudo-inverse of the projection matrix. Note that since the reconstruction matrices also only depend on the reference coordinates, they can be precomputed for all elements and cached.

We now turn to deriving the integration weights $R_{\underline{i}}$ on the subcells. One simple option is using the *extended midpoint rule*:

$$\int_\Omega \underline{u}\, \mathrm{d}^3x \approx \Delta\xi\Delta\eta\Delta\zeta \sum_{\underline{i}} \underline{u}_{\underline{i}} J_{\underline{i}}, \tag{64}$$

which means $R_{\underline{i}} = \Delta\xi\Delta\eta\Delta\zeta$. However, this formula is only second-order accurate. To obtain a higher-order approximation, we need to find weights $R_{\underline{i}}$ that approximate the integral

$$\int_a^b f(x)\, \mathrm{d}x \approx \sum_{\underline{i}=0}^{n} R_{\underline{i}} f(x_{\underline{i}}).$$

We provide the weights $R_{\underline{i}}$ in appendix B.

5.2. Intercell fluxes

One approach to dealing with the intercell fluxes is to use the mortar method [60–63]. In the mortar method, the boundary correction terms and numerical fluxes are computed on a new mesh whose resolution is the greater of the two elements sharing the boundary. In practice, we have found this not to be necessary to achieve a stable scheme. This can be understood by noting that from a shock capturing perspective, violating conservation is only an issue at discontinuities. Wherever the solution is smooth, conservation violations converge away. Since the hybrid scheme switches from DG to FD *before* a shock enters an element by retaking the time (sub) step, and since discontinuities are inevitably always somewhat smeared in any shock capturing scheme, we have found that exact conservation is not required between a DG and FD grid. The lack of conservation arises from reconstructing the FD variables to the DG element's interface before computing G, rather than computing G on the FD cell faces and then reconstructing G. Note that not enforcing exact conservation at boundaries is merely an implementation convenience.

First, let us describe the element using FD. In this case, the neighbor input data to the boundary correction from the DG grid is projected onto the FD grid on the interface. Then the Riemann solver computes the boundary correction G, which is then used in the FD scheme. On the DG grid the FD scheme is used to reconstruct the neighboring data on the common interface from the subcell data. The reconstructed FD data is then reconstructed to the DG grid, that is, it is transferred from the FD to the DG grid on the interface. Finally, the boundary correction is computed on the DG grid. It is the reordering of the reconstruction and projection with the Riemann solver that violates conservation at the truncation error level. Note that the DG and FD solvers must use the same Riemann solver.

5.3. The a posteriori idea

In this section we will discuss how the *a posteriori* idea is implemented. For now, we will not concern ourselves with which TCI is used, just that one is used to detect troubled cells. We have several criteria that drive the design decision. Specifically,

- Only one communication between nearest neighbors is necessary per time (sub) step;
- Switching between DG and FD does not require additional communication and neighbor information;
- Exact conservation between neighboring elements can be enforced;
- Both substep (Runge–Kutta) and multi-step (Adams–Bashforth) time integrators are supported;

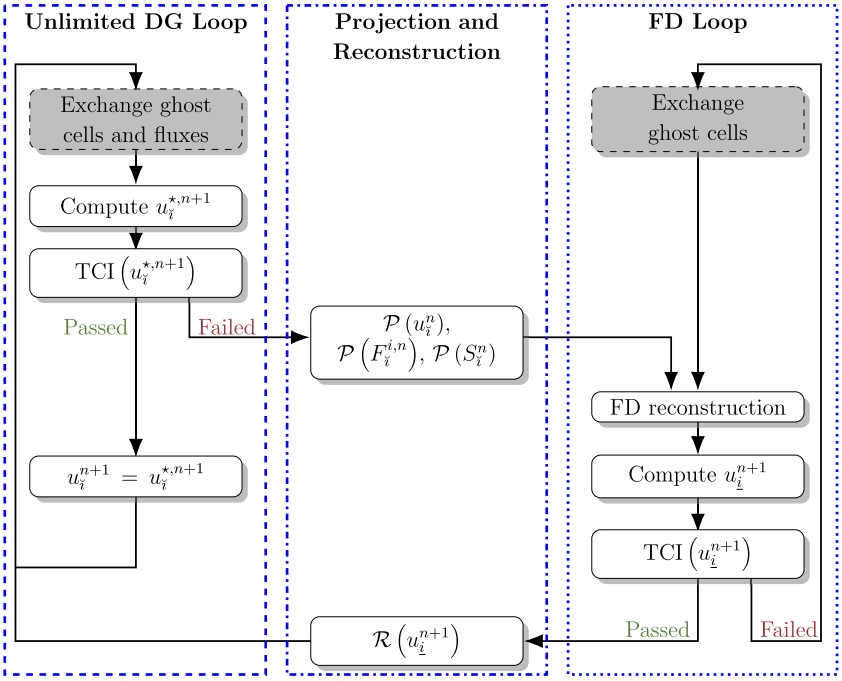

Figure 1. A schematic description of the proposed DG–FD hybrid method. We use superscripts n and $n+1$ to denote variables at time t^n and t^{n+1}. The unlimited DG loop, projection to and reconstructions from the FD subcells, and the FD loop are boxed to highlight how the hybrid scheme can be split into the unlimited DG and FD schemes with transformations (projection and reconstruction) that allow switching between the two methods. Steps that exchange data with neighboring elements are highlighted in light gray and have a dashed border. Specifically, these are 'exchange ghost cells and fluxes' and 'exchange ghost cells'.

- Physical realizability of the solution can be guaranteed.

We present a schematic of our DG–FD hybrid scheme in figure 1. The schematic has the unlimited DG loop on the left and the positivity-preserving FD loop on the right. Between them are the projection and reconstruction operations that allow the two schemes to work together and communicate data back and forth. The scheme starts in the 'unlimited DG loop' in the top left with a computation of the volume candidate. If the TCI finds the solution admissible the 'passed' branch is taken, otherwise the 'failed' branch is taken.

The algorithm proceeds as follows. We first compute a candidate solution $u^\star(t^{n+1})$ at time t^{n+1} using an unlimited DG scheme. The TCI is then used to check whether or not the candidate solution $u^\star(t^{n+1})$ is admissible. The TCI may depend on the candidate solution, the solution at the current time $u(t^n)$ within the element, and the solution in neighboring elements at time t^n. In order to minimize communication between elements, the TCI may not depend on the candidate solution in neighboring elements. If the candidate solution is found to be admissible by the TCI, we use it as the solution at t^{n+1}. That is, $u(t^{n+1}) = u^\star(t^{n+1})$. If the candidate solution is inadmissible, then we redo the time step using the FD subcells. In this case, the solution at t^n and the time stepper history (the time derivatives $\partial_t u(t^{n-1})$, etc) are projected onto the subcells, FD reconstruction is performed, data for the boundary correction/Riemann solver at the element boundaries is overwritten by projecting the DG solution to the FD grid

on the element boundaries, and the FD scheme takes the time step. Overwriting the FD reconstructed data $u_{\mathrm{FD}}^{\mathrm{interface}}$ with the projected DG solution $\mathcal{P}(u_{\mathrm{DG}}^{\mathrm{interface}})$ on the interfaces makes the scheme conservative when retaking the time step. Since the scheme is switching from DG to FD, it is likely a discontinuity is present and conservation is important. This ultimately means that neighboring elements are not aware that the element switched from DG to FD between times t^n and t^{n+1} until boundary data for time t^{n+1} is exchanged. Since the DG solution at time t^n is admissible, projecting it to the FD interface grid will be acceptable in nearly all cases. In cases where this projection leads to an unphysical solution, all elements sharing the interface can detect this and switch to FD; however, we have not yet implemented this. We now describe in detail how the algorithm is implemented in terms of communication patterns and parallelization.

First consider an element using DG. We start by computing the local contributions to the time derivative, the fluxes, source terms, non-conservative terms, and flux divergence. We store $\partial_t u$, compute local contributions to the boundary correction G, and then send our contributions to the boundary correction as well as the ghost cells of the primitive variables used for FD reconstruction to neighboring elements, as well as the interface mesh used to inform the neighbor that we are using DG. By sending both the inputs to the boundary correction and the data for FD reconstruction, we reduce the number of times communication is necessary. This is important since generally it is the number of times data is communicated not the amount of data communicated that causes a bottleneck. Once all contributions to the Riemann problem are received from neighboring elements, we compute the boundary correction and compute the candidate solution $u^\star(t^{n+1})$. We then apply the TCI described in section 5.4 below. If the cell is marked as troubled we undo the last timestep/substep and retake the timestep/substep using the FD method[3]. FD reconstruction is performed, but the projected boundary correction from the DG solve is used to ensure conservation between neighboring elements using FD. If the cell was not marked as troubled, we accept the candidate solution as being valid and take the next timestep/substep.

The FD solver starts by sending the data necessary for FD reconstruction to neighboring elements, including the interface mesh used to inform the neighbor that FD is being used. This means any neighboring elements doing DG need to reconstruct the inputs into the boundary correction using FD reconstruction. However, this allows us to maintain a single communication per time step, unlike traditional limiting strategies which inherently need two communications per time step. Once all FD reconstruction and boundary correction data has been received from neighboring elements, a FD time step is taken. Any DG boundary correction data is projected to the FD grid in order to reduce conservation violations at element boundaries. With the FD time step complete, we apply a TCI to see if the DG solution would be admissible. In both Runge–Kutta and multi-step methods, care is taken so as to not introduce discontinuities into the solution because they were present in past timesteps or substeps. In the case of Runge–Kutta time stepping we only switch back to DG at the end of a complete time step in order to avoid reconstructing discontinuities in the time stepper history to the DG grid. When multi-step methods are used, we wait until the TCI has marked enough time steps as being representable on the DG grid so that any discontinuities have cleared the time stepper history. For example, when using a third-order multi-step method the TCI needs to deem three time steps as representable on the DG grid before we switch to DG. For the multi-step method we apply the reconstruction operator $\mathcal{R}$ to the time stepper history ($\partial_t u(t^{n-1})$ etc).

[3] Note that only the most recent substep is retaken if a substep time integrator is being used.

5.4. Troubled-cell indicators

One of the most important parts of the DG–FD hybrid method is the TCI that determines when to switch from DG to FD. In [12] a numerical indicator based on the behavior of the polynomials representing the solution was used as well as physical indicators such as the density or pressure becoming negative. We believe that the combination of numerical and physical indicators is crucial, since it enables the development of non-oscillatory methods that also guarantee physical realizability of the solution. We will first outline the numerical indicator in this section. Then we will give a detailed description of the TCIs we use with the GRMHD system for the initial data, determining when to switch from DG to FD, and when to switch from FD back to DG.

The numerical indicator used in [12] is a relaxed discrete maximum principle (RDMP). The RDMP is a two-time-level indicator in the sense that it compares the candidate at t^{n+1} to the solution at time t^n. The RDMP requires that

$$\min_{\mathcal{N}}\left[u(t^n)\right] - \delta \leqslant u^\star(t^{n+1}) \leqslant \max_{\mathcal{N}}\left[u(t^n)\right] + \delta, \tag{65}$$

where $\mathcal{N}$ are either the Neumann or Voronoi neighbors plus the element itself, δ is a parameter defined below that relaxes the discrete maximum principle, and u are the conserved variables[4]. When computing $\max(u)$ and $\min(u)$ over an element using DG, we first project the DG solution to the subcells and then compute the maximum and minimum over *both* the DG solution and the projected subcell solution. However, when an element is using FD we compute the maximum and minimum over the subcells only. Note that the maximum and minimum values of $u^\star$ are computed in the same manner as those of u. The parameter δ used to relax the discrete maximum principle is given by:

$$\delta = \max\left(\delta_0, \epsilon\left\{\max_{\mathcal{N}}\left[u(t^n)\right] - \min_{\mathcal{N}}\left[u(t^n)\right]\right\}\right), \tag{66}$$

where, as in [12], we take $\delta_0 = 10^{-7}$ and $\epsilon = 10^{-3}$.

We have found that the RDMP TCI is not able to handle slow-moving shocks. This is precisely because it is a two-time-level TCI and measures the change in the solution from one time step to the next. Since discontinuities are inevitably still somewhat smeared with a FD scheme, a discontinuity moving slowly enough gradually generates large oscillations inside the element it is entering. The RDMP, measuring relative changes, does not react quickly enough or at all, and so the DG method ends up being used in elements with discontinuities. We demonstrate this below in the simple context of a 1D Burgers step solution with the mesh moving at nearly the speed of the discontinuity.

Since using the RDMP means we are unable to satisfy requirements 4.1(f) and (g), we seek a supplementary TCI to deal with these cases. We use the TCI proposed in [64], which we will refer to as the Persson TCI. This TCI looks at the falloff of the spectral coefficients of the solution, effectively comparing the power in the highest mode to the total power of the solution. Consider a discontinuity sensing quantity U, which is typically a scalar but could be a tensor of any rank. Let U have the 1D spectral decomposition:

$$U(x) = \sum_{i=0}^{N} c_i P_i(x), \tag{67}$$

[4] Any choice of quantities can be monitored.

where in our case $P_i(x)$ are Legendre polynomials, and c_i are the spectral coefficients[5]. We then define a filtered solution $\hat{U}$ as

$$\hat{U}(x) = c_N P_N(x). \tag{68}$$

The main goal of $\hat{U}$ is to measure how much power is in the highest mode, which is the mode most responsible for Gibbs phenomenon. In 2D and 3D we consider $\hat{U}$ on a dimension-by-dimension basis, taking the L_2 norm over the extra dimensions, reducing the discontinuity sensing problem to always being 1D. We define the discontinuity indicator s^Ω as

$$s^\Omega = \log_{10}\left(\frac{(\hat{U},\hat{U})}{(U,U)}\right), \tag{69}$$

where $(\cdot,\cdot)$ is an inner product, which we take to be the Euclidean L_2 norm (i.e. we do not divide by the number of grid points since that cancels out anyway).

We must now decide what values of s^Ω are large and therefore mean the DG solution is inadmissible. For a spectral expansion, we would like the solution to be at least continuous and so the spectral coefficients should decay at least as $1/N^2$ [65]. Since our sensor depends on the square of the coefficients, we expect at least $1/N^4$ decay for smooth solutions. With this in mind, we have found that requiring

$$s^\Omega < s^e = -\alpha_N \log_{10}(N+1), \tag{70}$$

with $\alpha_N = 4$ works well for detecting oscillations and switching to the FD scheme. In order to prevent rapid switching between the DG and FD schemes, we use $\alpha_N + 1$ for the TCI when deciding whether to switch back to DG.

5.4.1. Initial data TCI for GRMHD. We set the initial data on the DG grid, and then check a series of conditions to see if the initial data is representable on the DG grid. We require:

(a) That $\min(\tilde{D})$ over both the DG grid and the subcells is above a user-specified threshold. This is essentially a positivity check on $\tilde{D}$.
(b) That $\min(\tilde{\tau})$ over both the DG grid and the subcells is above a user-specified threshold. This is essentially a positivity check on $\tilde{\tau}$.
(c) That for all conserved variables their max and min on the subcells satisfies an RDMP compared to the max and min on the DG grid. The tolerances chosen are typically the same as those used for the two-level RDMP during the evolution.
(d) That $\tilde{D}$ and $\tilde{\tau}$ pass the Persson TCI.
(e) That if $\max\left(\sqrt{\tilde{B}^i \delta_{ij} \tilde{B}^j}\right)$ is above a user-specified threshold, $\sqrt{\tilde{B}^i \delta_{ij} \tilde{B}^j}$ satisfies the Persson TCI.

If all requirements are met, then the DG solution is admissible.

5.4.2. TCI on DG grid for GRMHD. On the DG grid we require:

(a) That the RDMP TCI passes.
(b) That $\min(\tilde{D})$ is above a user-specified threshold. This is essentially a positivity check. This is done over both the DG and projected subcell solution.

[5] When a filter is being used to prevent aliasing-driven instabilities, lower modes need to be included in $\hat{U}$. $\hat{U}$ should generally be the highest unfiltered mode.

(c) That $\min(\tilde{\tau})$ is above a user-specified threshold. This is essentially a positivity check. This is done over both the DG and projected subcell solution.
(d) That $\tilde{B}^2 \leqslant 1.0 - \epsilon_B 2\tilde{\tau}\sqrt{\gamma}$ at all grid points in the DG element.
(e) That primitive recovery is successful.
(f) That if we are in the atmosphere, we stay on DG. Since we have now recovered the primitive variables, we are able to say with certainty whether or not we are in atmosphere.
(g) That $\tilde{D}$ and $\tilde{\tau}$ pass the Persson TCI.
(h) That if $\max\left(\sqrt{\tilde{B}^i \delta_{ij} \tilde{B}^j}\right)$ is above a user-specified threshold, $\sqrt{\tilde{B}^i \delta_{ij} \tilde{B}^j}$ satisfies the Persson TCI.

If all requirements are met, then the DG solution is admissible.

5.4.3. TCI on FD grid for GRMHD. In order to switch to DG from FD, we require:

(a) That the RDMP TCI passes.
(b) That no conserved variable fixing was necessary. If the conserved variables needed to be adjusted in order to recover the primitive variables, then even the FD solution is inaccurate.
(c) That $\min(\tilde{D})$ is above a user-specified threshold. This is essentially a positivity check.
(d) That $\min(\tilde{\tau})$ is above a user-specified threshold. This is essentially a positivity check.
(e) That $\tilde{D}$ and $\tilde{\tau}$ pass the Persson TCI.
(f) That if $\max\left(\sqrt{\tilde{B}^i \delta_{ij} \tilde{B}^j}\right)$ is above a user-specified threshold, $\sqrt{\tilde{B}^i \delta_{ij} \tilde{B}^j}$ satisfies the Persson TCI.

If all the above checks are satisfied, then the numerical solution is representable on the DG grid.

5.5. On the number of subcells to use

The only hard requirement on the number of subcells used in 1D is $N_s \geqslant N + 1$ so that there are at least as many degrees of freedom to represent the solution on the subcells as there are in the DG scheme. However, the more optimal choice, as is argued in [12], is $N_s = 2N + 1$. This arises from comparing the time step size allowed when using a DG method, (43), to the time step size allowed when using a FV or FD method, (44). Choosing $N_s > 2N + 1$ is not desirable since that would result in having to take smaller time steps when switching from DG to FD. We refer the reader to section 4.5 of [12] for a more detailed discussion of the optimal number of subcells to use.

5.6. Perspective on DG–FD hybrid method

Given the complexity of the DG–FD hybrid scheme and the relative expense of FD schemes compared to the DG scheme, the DG–FD hybrid scheme might seem like a poor choice. We argue that this is not the case and that the hybrid scheme is actually a good choice. Consider needing a resolution of 130^d (very modest) to solve a problem using a FD scheme to a desired accuracy. The equivalent DG–FD hybrid scheme would use ten seventh-order elements so that in the worst case, where there are large discontinuities everywhere in the domain, the scheme is as accurate as the FD scheme. However, wherever the solution is smooth enough to be representable using DG, roughly 2^d fewer grid points are necessary. In 3D this makes a significant difference, especially if the numerical solution is representable using DG in much of the computational domain. For example, consider the case where half the elements are using FD. In

this case the DG–FD hybrid scheme uses ~ 0.58 times as many grid points as the equivalent FD scheme. Furthermore, the DG scheme only needs to solve the Riemann problem on element boundaries, and does not need to perform the expensive reconstruction step necessary in FD and FV schemes. Thus, the decrease in the number of grid points is a lower bound on the performance improvement the DG–FD hybrid scheme has to offer. Ultimately, we believe that the more useful view of the DG–FD hybrid scheme is that it is a FD scheme that uses DG as a way to compress the representation of the solution in smooth regions in order to increase efficiency.

6. Numerical results

6.1. Burgers equation: a slowly moving discontinuity

While extremely simple, Burgers equation allows us to easily test how well the RDMP and Persson TCI are able to handle slowly-moving discontinuities. Burgers' equation is given by

$$\partial_t U + \partial_x \left(\frac{U^2}{2} \right) = 0. \tag{71}$$

Whenever we use the Persson TCI we use the evolved variable U as the discontinuity sensing quantity.

We evolve the solution

$$U(x,t) = \begin{cases} 2 & \text{if } x \leqslant 0.25 + 1.5t \\ 1 & \text{otherwise} \end{cases} \tag{72}$$

on a moving mesh. The mesh has a velocity $v_g^x = 1.4$, while the discontinuity moves at speed 1.5. Thus, the discontinuity moves relatively slowly across the grid, allowing us to test how well each TCI handles such discontinuities. We integrate (71) using a third-order Adams–Bashforth time stepper, on an initial domain $x \in [-1, 1]$ with eight P_5 elements. We compare the RDMP TCI and the Persson TCI in figure 2 at a final time of $t_\mathrm{f} = 1.5$. The top row uses a time step of $\Delta t = 2.5 \times 10^{-3}$ and the bottom row uses $\Delta t = 5 \times 10^{-4}$. In all cases a third-order weighted compact nonlinear scheme is used for FD reconstruction. We use a Rusanov or local Lax–Friedrichs numerical flux/boundary correction.

The leftmost plot in the top row of figure 2 uses the Persson TCI with $\alpha_N = 3$, the center plot in the top row uses the Persson TCI with $\alpha_N = 4$, and the rightmost plot in the top row uses the RDMP TCI. We see that, in agreement with what is expected from a convergence analysis of Legendre polynomials [65], using $\alpha_N = 4$ to switch to the FD scheme is most robust as an indicator. We see that both the Persson TCI with $\alpha_N = 3$ and the RDMP TCI struggle to switch to the FD scheme quickly enough to prevent unphysical oscillations from entering the solution. In the bottom row of figure 2 we use a smaller time step size, $\Delta t = 5 \times 10^{-4}$, to make the relative change in U from one time step to the next smaller. From left to right we show results using the Persson TCI with $\alpha_N = 4$, the RDMP TCI, and the Persson TCI with $\alpha_N = 3$ alongside the RDMP TCI. In general, the RDMP is much better at preventing oscillations from appearing on the left of the discontinuity, while the Persson TCI does a better job on the right of the discontinuity. While interesting, it is unclear how this translates to more complex systems and flows. Although we cannot completely discount the RDMP, the Persson indicator does have an advantage in all cases, but using both TCIs together gives the best results. We ran the Persson TCI with $\alpha_N = 4$ alongside the RDMP TCI for the smaller time step case and found that

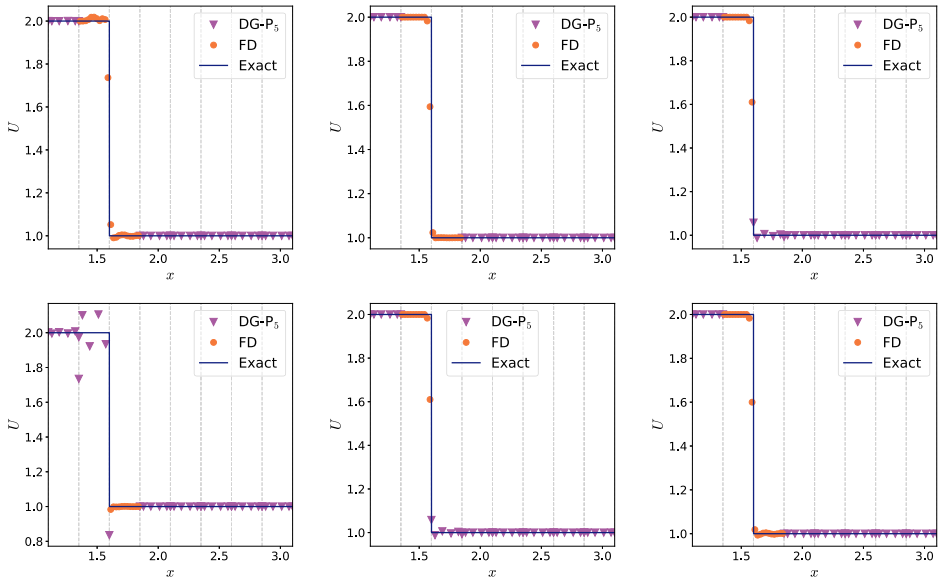

Figure 2. The step Burgers problem at $t_{\rm f} = 1.5$ using a DG–P_5 scheme hybridized with a WCNS3 FD scheme. A third-order Adams–Bashforth time stepper is used and the mesh is moving at velocity $v_g^x = 1.4$. Results in the top row are obtained using a time step size of $\Delta t = 2.5 \times 10^{-3}$ and in the bottom row using a time step size of $\Delta t = 5 \times 10^{-4}$. Going from left to right in the top row, the TCI used is the Persson TCI with $\alpha_N = 3$, the Persson TCI with $\alpha_N = 4$, and the RDMP TCI. Going from left to right in the bottom row, the TCI used is the Persson TCI with $\alpha_N = 3$, the RDMP TCI, and Persson TCI with $\alpha_N = 4$ along with the RDMP TCI.

no unphysical oscillations are visible, just as in the top middle plot of figure 2. We have verified that our results are the same whether using the SSP RK3 time stepper or the Adams–Bashforth time stepper.

6.2. General relativistic magnetohydrodynamics

In this section we present results of our DG–FD hybrid scheme when applied to various GRMHD test problems. The final test problem in this section is that of a single magnetized neutron star, demonstrating that our hybrid scheme is capable of simulating interesting relativistic astrophysics scenarios. We always use an HLL Riemann solver and typically the third-order strong-stability preserving Runge–Kutta (SSP RK3) time stepper [42]. However, we also compare a fifth-order Dormand–Prince method [66] to the RK3 method for some test problems. We mainly use the SSP RK3 stepper since this is a commonly used method when comparing shock capturing schemes. We also reconstruct the variables $\{\rho, p, Wv^i, B^i, \Phi\}$ using a monotonised central reconstruction scheme. We choose the resolution for the different problems by having the number of FD grid points be approximately equal to the number of grid points used by current production FD codes. Unless stated otherwise, we do not monitor $\tilde{B}^i$ with the Persson indicator since in most of the test cases we look at the magnetic field has discontinuities at or near the same place the fluid variables have discontinuities. All simulations use `SpECTRE` v2022.04.04 [33] and the input files are available as part of the arXiv version of this paper.

Table 1. The errors and local convergence order for the smooth flow problem using different limiting strategies. Note that the limiter is not applied if the TCI determines the DG solution to be valid. We observe the expected convergence rate except when the solution is underresolved because too few elements are used or when the error is no longer dominated by the truncation error of the DG scheme.

Method	N_x	$L_2(\mathcal{E}(\rho))$	L_2 order
DG–FD P_3	2	$3.50\,983 \times 10^{-1}$	
	4	$1.22\,554 \times 10^{-1}$	1.52
	8	$3.72\,266 \times 10^{-4}$	8.36
	16	$1.61\,635 \times 10^{-5}$	4.53
	32	$9.76\,927 \times 10^{-7}$	4.05
DG–FD P_4	2	$3.62\,426 \times 10^{-1}$	
	4	$3.79\,759 \times 10^{-4}$	9.90
	8	$1.15\,193 \times 10^{-5}$	5.04
	16	$3.73\,055 \times 10^{-7}$	4.95
DG–FD P_5	2	$3.45\,679 \times 10^{-1}$	
	4	$2.23\,822 \times 10^{-5}$	13.91
	8	$3.18\,504 \times 10^{-7}$	6.13
	16	$5.08\,821 \times 10^{-9}$	5.97

Table 2. The initial conditions for Riemann problems 1, 3, and 4 of [67]. The domain is $x \in [-0.5, 0.5]$, the final time is $t_\mathrm{f} = 0.4$, and an ideal fluid equation of state is used with an adiabatic index of 2 for Riemann problem 1 and $5/3$ for Riemann problems 3 and 4.

Problem		ρ	p	v^i	B^i
RP 1	$x < 0$	1.0	1.0	$(0.0, 0, 0)$	$(0.5, 1.0, 0.0)$
	$x \geqslant 0$	0.125	0.1	$(0.0, 0, 0)$	$(0.5, -1.0, 0.0)$
RP 3	$x < 0$	1.0	1000.0	$(0.0, 0, 0)$	$(10.0, 7.0, 7.0)$
	$x \geqslant 0$	1.0	0.1	$(0.0, 0, 0)$	$(10.0, 0.7, 0.7)$
RP 4	$x < 0$	1.0	0.1	$(0.999, 0, 0)$	$(10.0, 7.0, 7.0)$
	$x \geqslant 0$	1.0	0.1	$(-0.999, 0, 0)$	$(10.0, -7.0, -7.0)$

6.2.1. 1D smooth flow. We consider a simple 1D smooth flow problem to test which of the limiters and TCIs are able to solve a smooth problem without degrading the order of accuracy. A smooth density perturbation is advected across the domain with a velocity v^i. The analytic solution is given by

$$\rho = 1 + 0.7\,\sin[k^i(x^i - v^i t)], \tag{73}$$

$$v^i = (0.8, 0, 0), \tag{74}$$

$$k^i = (1, 0, 0), \tag{75}$$

$$p = 1, \tag{76}$$

$$B^i = (0, 0, 0), \tag{77}$$

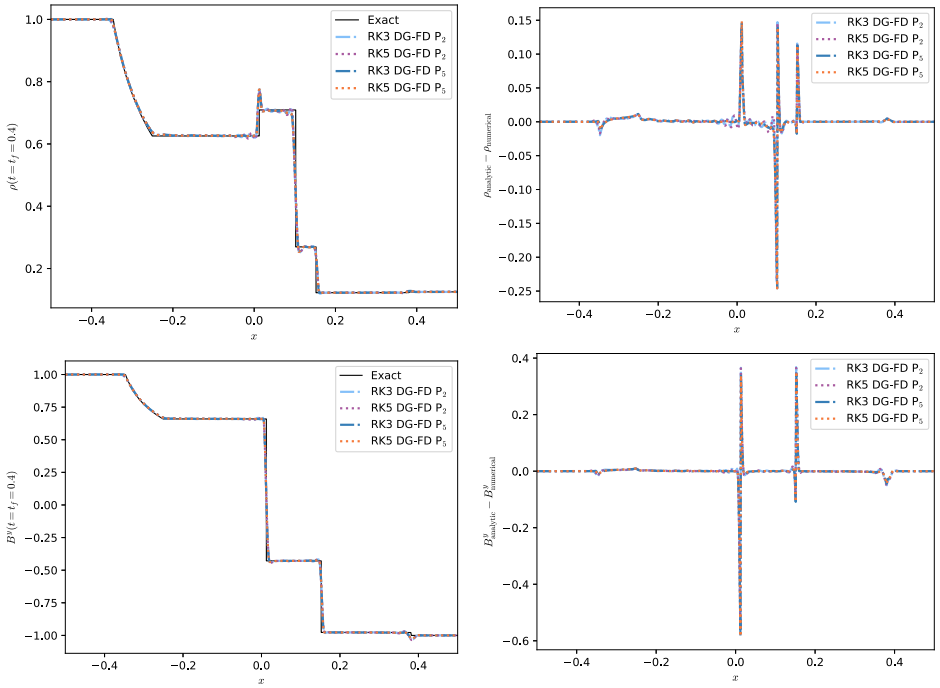

Figure 3. Results from Riemann problem 1 of [67] using a P_5 (64 elements) and P_2 (128 elements) DG–FD hybrid scheme with an SSP RK3 and Dormand–Prince five time stepper. All results are at the final time $t = 0.4$. The top left panel shows the rest mass density ρ, the bottom left the magnetic field B^y, and the right panels show the difference between the analytic and numerical solution. The P_5 scheme is able to resolve the discontinuities just as well as the P_2 scheme, while also admitting fewer unphysical oscillations away from the discontinuities.

and we close the system with an adiabatic equation of state,

$$p = \rho\epsilon(\Gamma - 1), \tag{78}$$

where Γ is the adiabatic index, which we set to 1.4. We use a domain given by $[0, 2\pi]^3$, and apply periodic boundary conditions in all directions. The time step size is $\Delta t = 2\pi/5120$ so that the spatial discretization error is larger than the time stepping error for all resolutions that we use.

We perform convergence tests at different DG orders and present the results in table 1. We show both the L_2 norm of the error and the convergence rate. The L_2 norm is defined as

$$L_2(u) = \sqrt{\frac{1}{M}\sum_{i=0}^{M-1} u_i^2}, \tag{79}$$

where M is the total number of grid points and u_i is the value of u at grid point i and the convergence order is given by

$$L_2 \text{ order} = \log_2\left[\frac{L_2(\mathcal{E}_{N_x/2})}{L_2(\mathcal{E}_{N_x})}\right]. \tag{80}$$

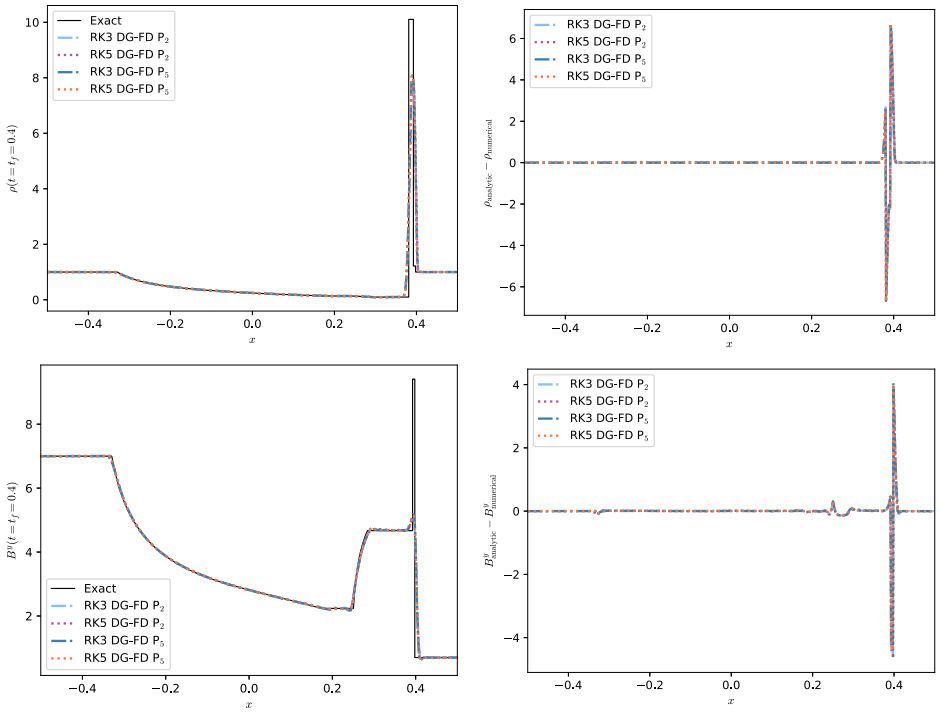

Figure 4. Results from Riemann problem 3 of [67] using a P_5 (64 elements) and P_2 (128 elements) DG–FD hybrid scheme with an SSP RK3 and Dormand–Prince five time stepper. All results are at the final time $t = 0.4$. The top left panel shows the rest mass density ρ, the bottom left the magnetic field B^y, and the right panels show the difference between the analytic and numerical solution. The P_5 scheme is able to resolve the discontinuities just as well as the P_2 scheme, while also admitting fewer unphysical oscillations away from the discontinuities.

We find that when very few elements are used, the TCI decides the solution is not well represented on the DG grid. Although if we disable the FD scheme completely, we find the DG method is stable, we find it acceptable that the TCI switches to FD in order to ensure robustness. Ultimately we observe the expected rate of convergence for smooth problems.

6.2.2. 1D Riemann problems. One-dimensional Riemann problems are a standard test for any scheme that must be able to handle shocks. We will focus on the first, third, and fourth Riemann problems (RP1, RP3, RP4) of [67]. The setup is given in table 2. We perform simulations using an SSP RK3 and a Dormand–Prince five method with $\Delta t = 5 \times 10^{-4}$. In the top left panels of figures 3–5 we show the rest mass density ρ at $t_\mathrm{f} = 0.4$, the bottom left panels show B^y, while the right panels show the difference between the analytic and numerical solution. The thin black curve is the analytic solution obtained using the Riemann solver of [68]. An ideal fluid equation of state (78) is used.

Impressively, the DG–FD hybrid scheme actually has fewer oscillations when going to higher order. In the right panels of figures 3–5 we plot the error of the numerical solution using a P_2 DG–FD scheme with 128 elements and a P_5 DG–FD scheme with 64 elements. We see that the P_5 hybrid scheme actually has fewer oscillations than the P_2 scheme, while resolving the discontinuities equally well. We attribute this to the TCIs triggering earlier when

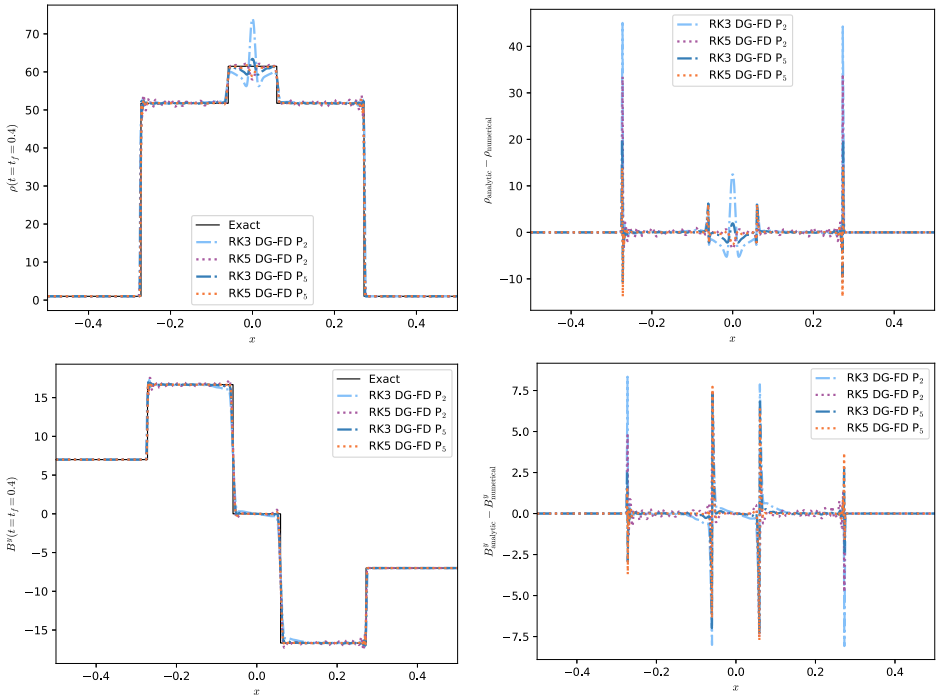

Figure 5. Results from Riemann problem 4 of [67] using a P_5 (64 elements) and P_2 (128 elements) DG–FD hybrid scheme with an SSP RK3 and Dormand–Prince five time stepper. All results are at the final time $t = 0.4$. The top left panel shows the rest mass density ρ, the bottom left the magnetic field B^y, and the right panels show the difference between the analytic and numerical solution. The P_5 scheme is able to resolve the discontinuities just as well as the P_2 scheme, while also admitting fewer unphysical oscillations away from the discontinuities.

a higher polynomial degree is used since discontinuities entering an element rapidly dump energy into the high modes. While the optimal order is almost certainly problem-dependent, given that current numerical relativity codes are mostly second order, achieving sixth order in the smooth regions is promising. The SSP RK3 time stepper seems to generally result in fewer oscillations than the Dormand–Prince five time stepper. This could stem from the Dormand–Prince stepper not being strong stability preserving. We leave a detailed comparison of different time integration schemes to future work.

6.2.3. 2D cylindrical blast wave. A standard test problem for GRMHD codes is the cylindrical blast wave [69, 70] where a magnetized fluid initially at rest in a constant magnetic field along the x-axis is evolved. The fluid obeys the ideal fluid equation of state with $\Gamma = 4/3$. The fluid begins in a cylindrically symmetric configuration, with hot, dense fluid in the region with cylindrical radius $r < 0.8$ surrounded by a cooler, less dense fluid in the region $r > 1$. The initial density ρ and pressure p of the fluid are

$$\rho(r < 0.8) = 10^{-2}, \tag{81}$$

$$\rho(r > 1.0) = 10^{-4}, \tag{82}$$

$$p(r < 0.8) = 1, \tag{83}$$

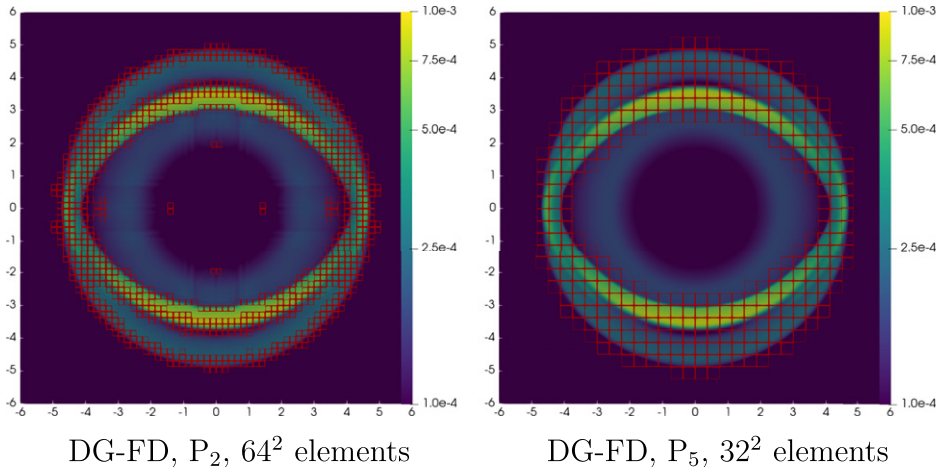

Figure 6. Cylindrical blast wave ρ at $t = 4$ showing the results of the using the DG–FD hybrid scheme with 64×64 P_2 elements (left) and 32×32 P_5 elements (right). The regions surrounded by maroon squares have switched from DG to FD.

$$p(r > 1.0) = 5 \times 10^{-4}. \tag{84}$$

In the region $0.8 \leqslant r \leqslant 1$, the solution transitions continuously and exponentially (i.e., transitions such that the logarithms of the pressure and density are linear functions of r). The fluid begins threaded with a uniform magnetic field with Cartesian components

$$(B^x, B^y, B^z) = (0.1, 0, 0). \tag{85}$$

The magnetic field causes the blast wave to expand non-axisymmetrically. For all simulations we use a time step size $\Delta t = 10^{-2}$ and an SSP RK3 time integrator.

We evolve the blast wave to time $t = 4.0$ on a grid of $64 \times 64 \times 1$ elements covering a cube of extent $[-6, 6]^3$ using a P_2 DG–FD scheme and on a grid of $32 \times 32 \times 1$ using a P_5 DG–FD scheme. With these choices the resolution when using FD everywhere is comparable to what FD codes use for this test. We apply periodic boundary conditions in all directions, since the explosion does not reach the outer boundary by $t = 4.0$. Figure 6 shows the logarithm of the rest-mass density at time $t = 4.0$, at the end of evolutions using the P_2 (left) and P_5 (right) DG–FD schemes. The increased resolution of a high-order scheme is clear when comparing the P_2 and P_5 solutions in the interior region of the blast wave. It is not clear that going to even higher order would be useful in this problem since to maintain the same time step size we would need to decrease the number of elements. Furthermore, as we can already see by comparing the P_2 and P_5 schemes, a greater area of the P_5 solution is using FD, though it is difficult to determine what overall effect this has, especially since high-order FD schemes could be used. We show the percentage of elements using FD instead of DG at the final time in table 3. As expected, the percentage of elements using FD decreases as the number of elements is increased.

6.2.4. 2D magnetic rotor. The second two-dimensional test problem we study is the magnetic rotor problem originally proposed for non-relativistic MHD [71, 72] and later generalized to the

Table 3. The percentage of elements using FD at the final time of the cylindrical blast wave simulation.

Method	Domain	Percent using FD (%)
DG–FD P_2	32^2	36.7
	64^2	22.9
	128^2	7.9
DG–FD P_5	16^2	57.8
	32^2	35.9
	64^2	21.8

relativistic case [73, 74]. A rapidly rotating dense fluid cylinder is inside a lower density fluid, with a uniform pressure and magnetic field everywhere. The magnetic braking will slow down the rotor over time, with an approximately 90 degree rotation by the final time $t = 0.4$. We use a domain of $[-0.5, 0.5]^3$ and a time step size $\Delta t = 10^{-3}$ and an SSP RK3 time integrator. An ideal fluid equation of state with $\Gamma = 5/3$ is used, and the following initial conditions are imposed:

$$p = 1 \tag{86}$$

$$B^i = (1, 0, 0) \tag{87}$$

$$v^i = \begin{cases} (-y\Omega, x\Omega, 0), & \text{if } r \leqslant R_{\text{rotor}} = 0.1 \\ (0, 0, 0), & \text{otherwise,} \end{cases} \tag{88}$$

$$\rho = \begin{cases} 10, & \text{if } r \leqslant R_{\text{rotor}} = 0.1 \\ 1, & \text{otherwise,} \end{cases} \tag{89}$$

with angular velocity $\Omega = 9.95$. The choice of Ω and $R_{\text{rotor}} = 0.1$ guarantees that the maximum velocity of the fluid (0.995) is less than the speed of light. We impose periodic boundary conditions.

We show the results of our evolutions using 64×64 P_2 elements (left) and 32×32 P_5 elements (right) in figure 7. Again, the DG–FD hybrid scheme is robust and accurate, though a fairly large number of cells end up being marked as troubled in this problem. However, using FD in more elements is not something we view as inherently bad, since we favor robustness in realistic simulations. The process of tweaking parameters and restarting simulations is both time consuming and frustrating, and so giving up some efficiency for robustness is preferable in general.

6.2.5. 2D magnetic loop advection. The last two-dimensional test problem we study is magnetic loop advection problem [75]. A magnetic loop is advected through the domain until it returns to its starting position. We use an initial configuration very similar to [40, 76–78], where

$$\rho = 1 \tag{90}$$

$$p = 3 \tag{91}$$

$$v^i = (1/1.2, 1/2.4, 0) \tag{92}$$

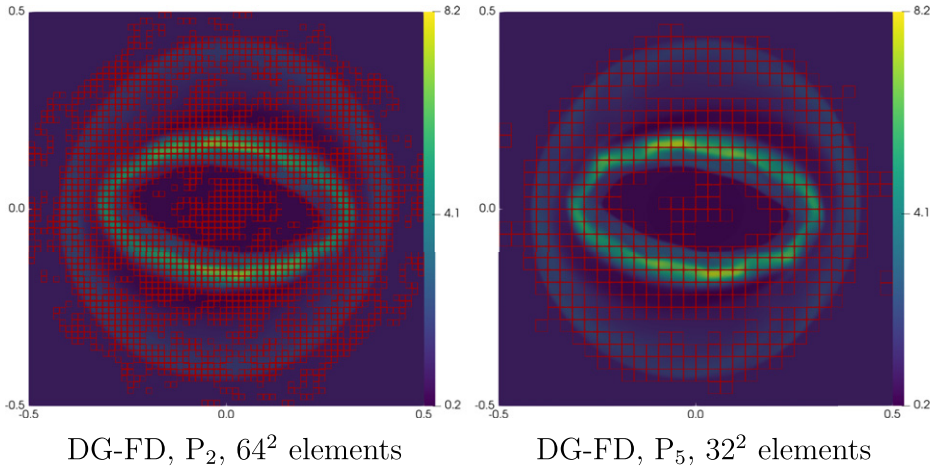

Figure 7. Magnetic rotor ρ at $t = 0.4$ showing the results of the using the DG–FD hybrid scheme with 64×64 P_2 elements (left) and 32×32 P_5 elements (right). The regions surrounded by maroon squares have switched from DG to FD.

$$B^x = \begin{cases} -A_{\text{loop}} y/R_{\text{in}}, & \text{if } r \leqslant R_{\text{in}} \\ -A_{\text{loop}} y/r, & \text{if } R_{\text{in}} < r < R_{\text{loop}} \\ 0, & \text{otherwise,} \end{cases} \tag{93}$$

$$B^y = \begin{cases} A_{\text{loop}} x/R_{\text{in}}, & \text{if } r \leqslant R_{\text{in}} \\ A_{\text{loop}} x/r, & \text{if } R_{\text{in}} < r < R_{\text{loop}} \\ 0, & \text{otherwise,} \end{cases} \tag{94}$$

with $R_{\text{loop}} = 0.3$, $R_{\text{in}} = 0.001$, and an ideal gas equation of state with $\Gamma = 5/3$. The computational domain is $[-0.5, 0.5]^3$ with $64 \times 64 \times 1$ elements and periodic boundary conditions being applied everywhere. The final time for one period is $t = 2.4$. For all simulations we use a time step size $\Delta t = 10^{-3}$ and an SSP RK3 time integrator. Since the fluid variables are smooth in this problem, we apply the Persson TCI to the Euclidean magnitude of $\tilde{B}^i$ in elements where the maximum value of the magnitude is above 10^{-5}.

In figure 8 we plot the magnetic field component B^x at $t = 0$ on the left half of each plot and after one period $t = 2.4$ on the right half of each plot. In the left panel of figure 8 we show the result using a P_2 DG–FD scheme and in the right panel of figure 8 using a P_5 DG–FD scheme. The P_5 scheme resolves the smooth parts of the solution more accurately than the P_2 scheme, as is to be expected. Finally, in figure 9 we plot the divergence cleaning field Φ at the final time $t = 2.4$. We do not observe any artifacts appearing in the divergence cleaning field at the interfaces between the DG and FD solvers, demonstrating that the divergence cleaning properties of the system are not adversely affected by using two different numerical methods.

6.2.6. TOV star. A rigorous 3D test case in general relativity is the evolution of a TOV star [79, 80]. In this section we study evolutions of both non-magnetized and magnetized TOV stars. We adopt the same configuration as in [81]. Specifically, we use a polytropic equation of

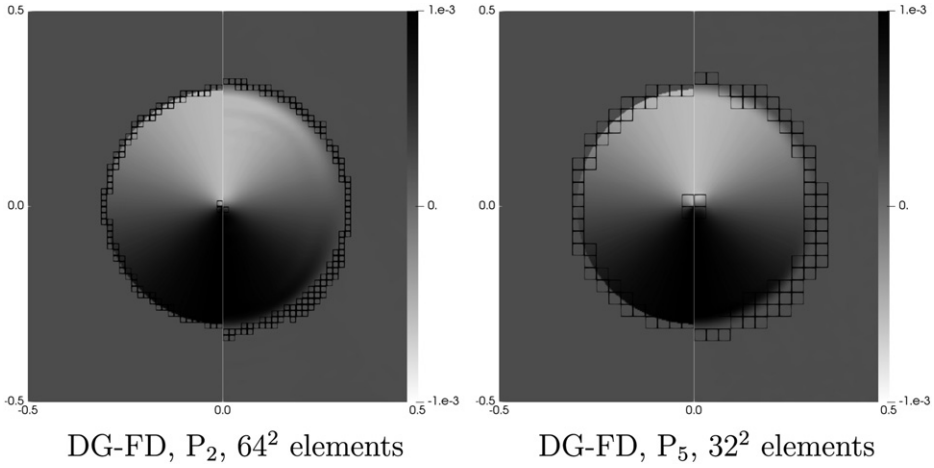

Figure 8. B^x for the magnetic loop advection problem. The left half of each plot is at the initial time, while the right half is after one period ($t = 2.4$). We show the results of the using the DG–FD hybrid scheme with 64×64 P_2 elements (left) and 32×32 P_5 elements (right). The regions surrounded by black squares have switched from DG to FD.

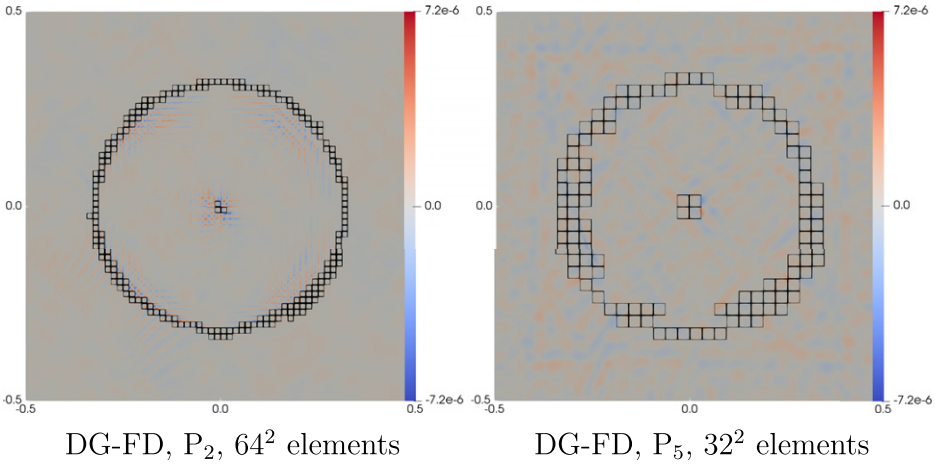

Figure 9. The divergence cleaning field Φ for the magnetic loop advection problem after one period ($t = 2.4$). We show the results of the using the DG–FD hybrid scheme with 64×64 P_2 elements (left) and 32×32 P_5 elements (right). The regions surrounded by black squares have switched from DG to FD.

state,

$$p(\rho) = K\rho^{\Gamma} \tag{95}$$

with the polytropic exponent $\Gamma = 2$, polytropic constant $K = 100$, and a central density $\rho_c = 1.28 \times 10^{-3}$. For the magnetized case, we choose a magnetic field given by a vector potential

$$A_\phi = A_b\left(x^2 + y^2\right) \max\left(p - p_{\rm cut}, 0\right)^{n_s}, \tag{96}$$

with $A_b = 2500$, $p_{\rm cut} = 0.04 p_{\rm max}$, and $n_s = 2$. This configuration yields a magnetic field strength in CGS units

$$|B_{\rm CGS}| = \sqrt{b^2} \times 8.352 \times 10^{19}\ {\rm G}, \tag{97}$$

of $|B_{\rm CGS}| = 1.03 \times 10^{16}\,{\rm G}$. The magnetic field is only a perturbation to the dynamics of the star, since $(p_{\rm mag}/p)(r = 0) \sim 5 \times 10^{-5}$. However, evolving the field stably and accurately can be challenging. The magnetic field corresponding to the vector potential in (96) in the magnetized region is given by

$$B^x = \frac{1}{\sqrt{\gamma}} \frac{xz}{r} A_b n_s (p - p_{\rm cut})^{n_s - 1} \partial_r p, \tag{98}$$

$$B^y = \frac{1}{\sqrt{\gamma}} \frac{yz}{r} A_b n_s (p - p_{\rm cut})^{n_s - 1} \partial_r p, \tag{99}$$

$$B^z = -\frac{A_b}{\sqrt{\gamma}} \left[2(p - p_{\rm cut})^{n_s} + \frac{x^2 + y^2}{r} n_s (p - p_{\rm cut})^{n_s - 1} \partial_r p \right], \tag{100}$$

and at $r = 0$ is

$$B^x = 0, \tag{101}$$

$$B^y = 0, \tag{102}$$

$$B^z = -\frac{A_b}{\sqrt{\gamma}} 2(p - p_{\rm cut})^{n_s}. \tag{103}$$

We perform all evolutions in full 3D with no symmetry assumptions and in the Cowling approximation, i.e., we do not evolve the spacetime. To match the resolution usually used in FD/FV numerical relativity codes, we use a domain $[-20, 20]^3$ with a base resolution of six P_5 DG elements. This choice means we have approximately 32 FD grid points covering the star's diameter at the lowest resolution, 64 when using twelve P_5 elements, and 128 grid points when using 24 P_5 elements. In all cases we set $\rho_{\rm atm} = 10^{-15}$ and $\rho_{\rm cutoff} = 1.01 \times 10^{-15}$. We do not run any simulations using a P_2 DG–FD hybrid scheme since the P_5 scheme has proven to be more accurate and robust in all test cases so far.

In the left panel of figure 10 we show the maximum rest mass density over the grid divided by the maximum density at $t = 0$ for the non-magnetized TOV star. The six-element simulation uses FD throughout the interior of the star because the corners of the inner elements are in vacuum. In comparison, the 12- and 24-element simulations use the unlimited P_5 DG solver throughout the star interior. The increased 'noise' in the 12- and 24-element data actually stems from the higher oscillation modes in the star [82] that are induced by numerical error. In the right panel of figure 10 we plot the power spectrum using data at the three different resolutions. The six-element simulation only has one mode resolved, while 12 elements resolve two modes well, and the 24-element simulation resolves three modes well. Additionally, we plot the power spectrum from a 24-element simulation using a fifth-order Dormand–Prince time stepper instead of the strong stability preserving third-order Runge–Kutta method. Increasing the time stepper order does not increase the number of radial modes resolved, demonstrating that it is the spatial resolution that is the limiting factor.

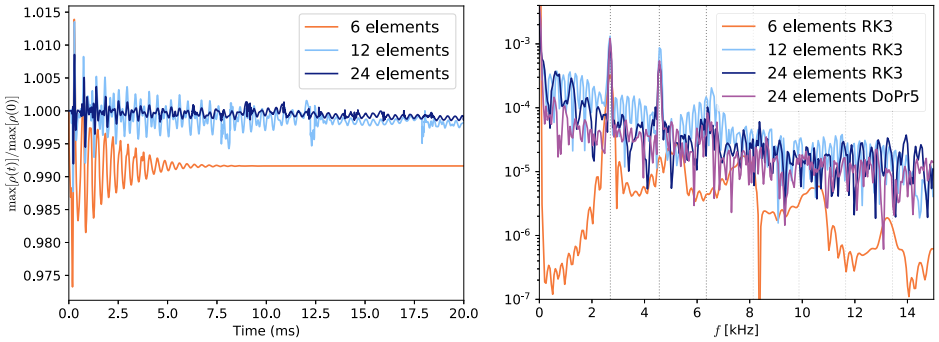

Figure 10. A plot of $\max[\rho(t)]/\max[\rho(0)]$ at three different resolution (left panel) for the non-magnetized TOV star. The six-element simulation uses FD throughout the interior of the star, while 12- and 24-element simulations use DG. The maximum density in the six-element case drifts down at early times because of the low resolution and the relatively low accuracy of using FD at the center. The power spectrum of the maximum density for the three different resolution is plotted in the right panel. The vertical dashed lines correspond to the known frequencies in the Cowling approximation [82]. When the high-order DG scheme is used, more oscillation frequencies are resolved. We also show the spectrum from a simulation using a fifth-order Dormand–Prince time stepper.

We show the normalized maximum rest mass density over the grid for the magnetized TOV star in the left panel of figure 11. Overall the results are nearly identical to the non-magnetized case. One notable difference is the decrease in the 12-element simulation between 7.5 ms and 11 ms, which occurs because the code switches from DG to FD at the center of the star at 7.5 ms and back to DG at 11 ms. Nevertheless, the frequencies are resolved just as well for the magnetized star as for the non-magnetized case, as can be seen in the right panel of figure 11 where we plot the power spectrum. Specifically, we are able to resolve the three largest modes with our P_5 DG–FD hybrid scheme. To the best of our knowledge, these are the first simulations of a magnetized neutron star using high-order DG methods.

6.2.7. Rotating neutron star. As a final test case we simulate a uniformly rotating neutron star with ratio of polar to equatorial radius of 0.7, similar to that of [82]. The initial data is constructed using the method described in [83, 84]. We use the same polytropic equation of state as for the TOV star evolution. In the left panel of figure 12 we show the maximum of the rest mass density for the same three resolutions used for the TOV star simulations. The lowest resolution uses FD throughout the star and sees a rapid decay in the density. The 12-element simulation uses DG throughout most of the interior of the star and so sees significant less decay in the density. The 24-element simulation uses DG everywhere in the interior of the star and sees less than a 0.1% decay in the density over 20 ms. To further test convergence we plot the maximum density of a 1 ms long 24-element and 48-element simulation in the right panel of figure 12. The oscillations continue to decrease with increasing resolution. We attribute the decay in the maximum density at lower resolutions to the dissipative nature of FD schemes, consistent with the rapid reduction in decay of the maximum density when switching to DG and increasing the resolution. These are also the first simulations of a rotating neutron star using high-order DG methods.

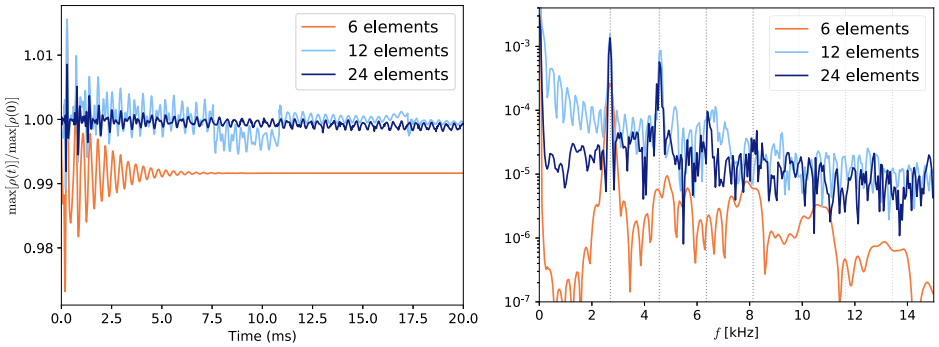

Figure 11. A plot of $\max[\rho(t)]/\max[\rho(0)]$ at three different resolution (left panel) for the magnetized TOV star. The six-element simulation uses FD throughout the interior of the star, while 12- and 24-element simulations use DG. The maximum density in the six-element case drifts down at early times because of the low resolution and the relatively low accuracy of using FD at the center. The power spectrum of the maximum density for the three different resolution is plotted in the right panel. The vertical dashed lines correspond to the known frequencies in the Cowling approximation (which are the same as the non-magnetized case as the magnetic field is a small perturbation on the dynamics). When the high-order DG scheme is used, more oscillation frequencies are resolved.

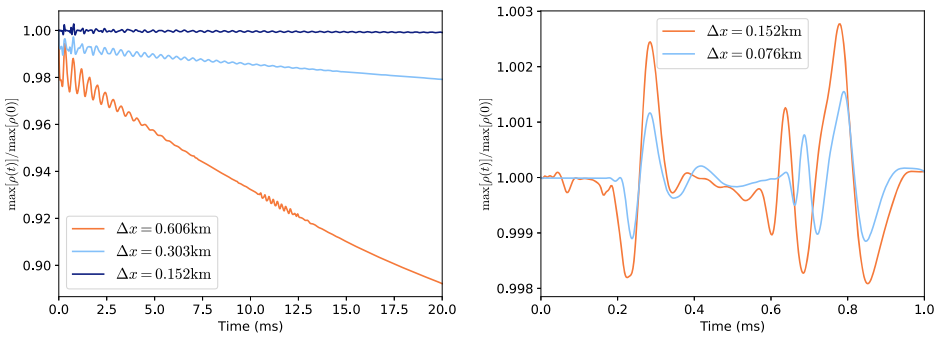

Figure 12. The left panel shows $\max[\rho(t)]/\max[\rho(0)]$ at three different resolution for the uniformly rotating neutron star. The six-element simulation uses FD throughout the interior of the star, the 12-element simulation uses mostly DG in the stellar interior, and the 24-element simulations use DG everywhere except the stellar surface. The right panel shows $\max[\rho(t)]/\max[\rho(0)]$ for a shorter period of time but at very high resolutions, 24 elements and 48 elements. Increasing from 24 to 48 elements further reduces oscillations in the maximum density.

7. Conclusions

In this paper we gave a detailed description of our DG–FD hybrid method that can successfully solve challenging relativistic astrophysics test problems like the simulation of a magnetized or rotating neutron star. Our method combines an unlimited DG solver with a conservative FD solver. Alternatively, this can be thought of as taking a standard FD code in numerical relativity and compressing the data to a DG grid wherever the solution is smooth. The DG solver is more efficient than the FD solver since no reconstruction is necessary and fewer Riemann

problems need to be solved. In theory a speedup of about eight is achievable, though we have not optimized our code `SpECTRE` [33] enough and so we find in practice a speedup of about two to three when comparing the hybrid method to using FD everywhere. The basic idea of the hybrid scheme is similar to [10–13]. An unlimited DG solver is used wherever a TCI deems the DG solution admissible, while a FD solver is used elsewhere. Unlike classical limiting strategies like WENO which attempt to filter out unphysical oscillations, the hybrid scheme prevents spurious oscillations from entering the solution. This is achieved by retaking any time step using a robust high-resolution shock-capturing conservative FD where the DG solution was inadmissible, either because the DG scheme produced unphysical results like negative densities or because a numerical criterion like the percentage of power in the highest modes deemed the DG solution bad. Our DG–FD hybrid scheme was used to perform what is to the best of our knowledge the first ever simulations of a magnetized TOV star and rotating neutron star using DG methods. In the future we plan to extend the hybrid scheme to curved meshes, simulations in full general relativity where the metric is evolved, and to use positivity-preserving adaptive-order FD methods in order to maintain the highest order possible even when using FD instead of DG.

Acknowledgments

Charm++/Converse [85] was developed by the Parallel Programming Laboratory in the Department of Computer Science at the University of Illinois at Urbana-Champaign. The figures in this article were produced with `matplotlib` [86, 87], `TikZ` [88] and `ParaView` [89, 90]. Computations were performed with the Wheeler cluster at Caltech. This work was supported in part by the Sherman Fairchild Foundation and by NSF Grant Nos. PHY-2011961, PHY-2011968, and OAC-1931266 at Caltech, and NSF Grant Nos. PHY-1912081 and OAC-1931280 at Cornell.

Data availability statement

The input files are available as part of the arXiv version of this paper.

Appendix A. Curved hexahedral elements and moving meshes

We have not yet implemented support for curved hexahedral meshes into SpECTRE. However, we have given careful consideration on how they could be implemented. In this appendix we discuss two possible implementations, one that requires many additional ghost cells with dimension-by-dimension reconstruction, and one that requires multidimensional reconstruction but no additional ghost cells.

Support for curved hexahedral or rectangular meshes can be achieved by combining the DG scheme with a multipatch or multidomain FD scheme. We will discuss only the 2D case, since the 3D case has more tedious bookkeeping, but otherwise is a straightforward extension. As a concrete example, we consider a 2D disk made out of a square surrounded by four wedges as shown in figure A1. We focus on an element at the top right corner of the central square and its neighbors, highlighted by the dashed squared in figure A1. We will first discuss how to handle the boundaries when a pair of neighboring elements are using the FD scheme, and then consider the case when one element is using DG and the other FD.

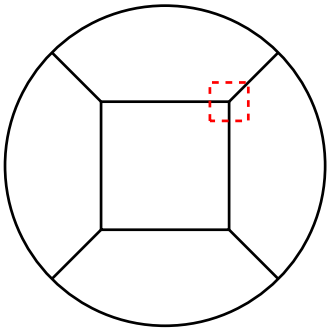

Figure A1. A 2D disk made out of a central square surrounded by four wedges. In the text we describe the method of handling intercell fluxes for the elements inside the dashed square.

In figure A2 we illustrate the domain setup, showing the subcell center points as circles in the two elements of interest. The diamonds in left panel of figure A2 represent the ghost cells needed for reconstruction to the element boundary in the element on the right. We use diagonal dotted lines to trace out lines of constant reference coordinates in the element on the right and dashed lines in the element on the left. Notice that the dashed and dotted lines intersect on the element boundary. This is because the mapping from the reference frame is continuous across element boundaries and allows us to have a conservative scheme using centered stencils even in the multipatch case.

Since we are unable to interpolate to the ghost cells shown in the left panel of figure A2 with centered stencils, one option is to use non-centered stencils. Using non-centered stencils was explored in reference [91], which did not find any instabilities from the use of such stencils in their test cases. Another option is to use reconstruction methods for unstructured meshes (see, for example, [92–97] and references therein), though this adds significant conceptual and technical overhead. Another option is adding additional subcells that overlap with the neighboring elements to allow the use of centered reconstruction schemes to interpolate to the ghost cells. These additional subcells are shown as triangles in the middle panel of figure A2. We can now do two reconstructions to reconstruct the ghost cells. First, we reconstruct along one reference axis of the central element as shown by the squares in the right panel of figure A2. Next we reconstruct along the other direction, which is illustrated by the dotted vertical line in the right panel of figure A2.

In order to maintain conservation between elements, we need to define a unique left and right state at the boundary of the elements. A unique state can be obtained by using the average of the reconstructed variables from the diagonal and horizontal stencils in figure A2. That is, we use the average of the result obtained from reconstruction in each element for the right and left states when updating any subcells that need the numerical flux on the element boundaries. Recall that when using a second-order FD derivative the semi-discrete evolution equations are (we only show 1D for simplicity since it is sufficient to illustrate our point)

$$\partial_t u + \frac{\partial \xi}{\partial x}\left(\frac{\hat{F}^x_{\underline{i}+1/2,\underline{j}} - \hat{F}^x_{\underline{i}-1/2,\underline{j}}}{\Delta\xi}\right) = S. \tag{A.1}$$

Thus, as long as all cells that share the boundary on which the numerical fluxes are defined use the same numerical flux, the scheme is conservative. When using higher-order derivative

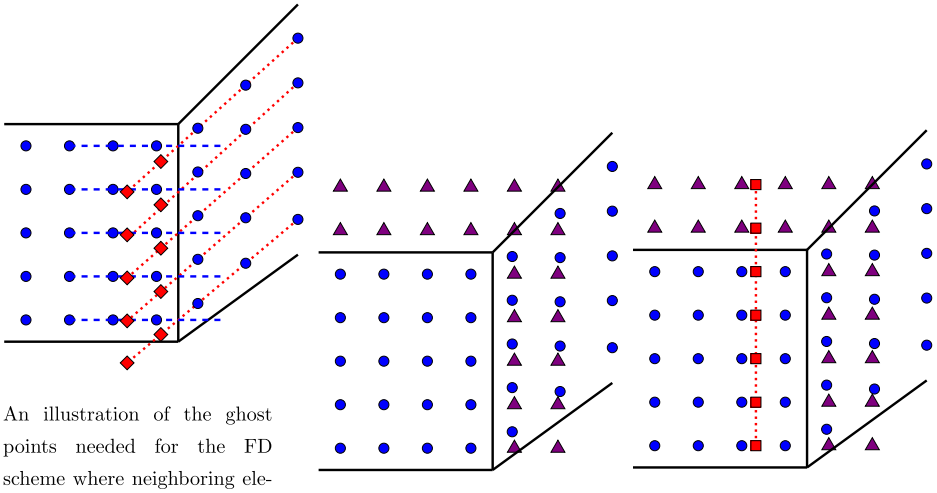

An illustration of the ghost points needed for the FD scheme where neighboring elements do not have aligned coordinate axes in their reference frames. Circles denote the cell-center FD points in the elements, and diamonds denote the ghost cells needed for reconstruction in the element on the right. The diagonal dotted lines trace out lines of constant reference coordinates in the element on the right, and dashed lines in the element on the left. Notice that the dashed and dotted lines intersect on the element boundary.

An illustration of extending the FD element by additional cells in order to support high-order reconstruction to arbitrary points inside the element, as discussed in the text. The additional cells for the central element are shown as purple triangles. These additional cells are evolved alongside the cells inside the element.

An illustration of the first stage of the reconstruction to the ghost cells needed by the neighboring element on the right. The central element reconstructs the solution to a line in the reference coordinates, followed by a second reconstruction to the ghost cells that fall on the line (not shown for simplicity).

Figure A2. An illustration of the multipatch or multidomain FD reconstruction needed to support curved meshes. We show a 2D example for simplicity. The 3D case is a tedious but otherwise straightforward generalization.

approximations the fluxes away from the cell boundaries are also needed. In the case of the element boundaries we are considering, we do not have a unique solution in the region of overlap (e.g. the region covered by the purple triangles in the middle panel of figure A2) where we compute the fluxes. As a result, we do not know if using high-order FD derivatives would violate conservation at the element boundaries. However, if the solution is smooth in this region, small violations of conservation are not detrimental, and if a discontinuity is passing through the boundary a second-order FD derivative should be used anyway.

Another method of doing reconstruction at locations where the coordinate axes do not align is described in [98] for FV methods. This same approach should be applicable to FD methods. Whether adding ghost zones or using unstructured mesh reconstruction is easier to implement and more efficient is unclear and will need to be tested.

Table B1. Weights for a fourth-order approximation to an integral using stencils symmetric about the center. Only the first half of the coefficients are shown, the second half are such that the stencil is symmetric. The number of points in the stencil is shown in the first column.

Number of cells	$x_{1/2}$	$x_{3/2}$	$x_{5/2}$	$x_{7/2}$	$x_{9/2}$
3	$\frac{9}{8}$	$\frac{3}{4}$	—	—	—
4	$\frac{13}{12}$	$\frac{11}{12}$	—	—	—
5	$\frac{13}{12}$	$\frac{21}{24}$	$\frac{13}{12}$	—	—
6	$\frac{9}{8}$	$\frac{3}{4}$	$\frac{9}{8}$	—	—
7	$\frac{9}{8}$	$\frac{3}{4}$	$\frac{7}{6}$	$\frac{11}{12}$	—
8	$\frac{9}{8}$	$\frac{3}{4}$	$\frac{7}{6}$	$\frac{23}{24}$	—
9+	$\frac{9}{8}$	$\frac{3}{4}$	$\frac{7}{6}$	$\frac{23}{24}$	1

Table B2. Weights for a sixth-order approximation to an integral using stencils symmetric about the center. Only the first half of the coefficients are shown, the second half are such that the stencil is symmetric. The number of points in the stencil is shown in the first column.

Number of cells	$x_{1/2}$	$x_{3/2}$	$x_{5/2}$	$x_{7/2}$	$x_{9/2}$	$x_{11/2}$	$x_{13/2}$	$x_{15/2}$
5	$\frac{1375}{1152}$	$\frac{125}{288}$	$\frac{335}{192}$	—	—	—	—	—
6	$\frac{741}{640}$	$\frac{417}{640}$	$\frac{381}{320}$	—	—	—	—	—
7	$\frac{741}{640}$	$\frac{3547}{5760}$	$\frac{8111}{5760}$	$\frac{611}{960}$	—	—	—	—
8	$\frac{1663}{1440}$	$\frac{227}{360}$	$\frac{323}{240}$	$\frac{139}{160}$	—	—	—	—
9	$\frac{1663}{1440}$	$\frac{227}{360}$	$\frac{1547}{1152}$	$\frac{245}{288}$	$\frac{3001}{2880}$	—	—	—
10	$\frac{1375}{1152}$	$\frac{125}{288}$	$\frac{335}{192}$	$\frac{125}{288}$	$\frac{1375}{1152}$	—	—	—
11	$\frac{1375}{1152}$	$\frac{125}{288}$	$\frac{335}{192}$	$\frac{2483}{5760}$	$\frac{7183}{5760}$	$\frac{863}{960}$	—	—
12	$\frac{1375}{1152}$	$\frac{125}{288}$	$\frac{335}{192}$	$\frac{2483}{5760}$	$\frac{3583}{2880}$	$\frac{2743}{2880}$	—	—
13	$\frac{1375}{1152}$	$\frac{125}{288}$	$\frac{335}{192}$	$\frac{2483}{5760}$	$\frac{3583}{2880}$	$\frac{1823}{1920}$	$\frac{2897}{2880}$	—
14	$\frac{1375}{1152}$	$\frac{125}{288}$	$\frac{335}{192}$	$\frac{2483}{5760}$	$\frac{3583}{2880}$	$\frac{1823}{1920}$	$\frac{5777}{5760}$	—
15+	$\frac{1375}{1152}$	$\frac{125}{288}$	$\frac{335}{192}$	$\frac{2483}{5760}$	$\frac{3583}{2880}$	$\frac{1823}{1920}$	$\frac{5777}{5760}$	1

Appendix B. Integration weights

The standard weights available in textbooks assume the abscissas are distributed at the boundaries of the subcells, not the subcell centers, and so do not apply. The weights $R_{\underline{i}}$ are given by integrals over Lagrange polynomials:

$$R_{\underline{i}} = \int_a^b \prod_{\substack{\underline{j}=0 \\ \underline{j}\neq\underline{i}}}^{n} \frac{(x - x_{\underline{j}})}{(x_{\underline{i}} - x_{\underline{j}})}\,\mathrm{d}x. \tag{B.1}$$

The integration coefficients are not unique since there are choices on how to handle points near the boundaries and how to stitch the interior solution together. Rather than using one-sided or low-order centered stencils near the boundaries, we choose to integrate from 0 to $3\Delta x$ for the

fourth-order stencil and from 0 to $5\Delta x$ for the sixth-order stencils. The fourth-order stencil at the boundary is

$$\int_0^{3\Delta x} f(x)\mathrm{d}x \approx \Delta x\left(\frac{9}{8}f_{1/2} + \frac{3}{4}f_{3/2} + \frac{9}{8}f_{5/2}\right), \tag{B.2}$$

and the sixth-order stencil is

$$\int_0^{5\Delta x} f(x)\mathrm{d}x \approx \Delta x\left(\frac{1375}{1152}f_{1/2} + \frac{125}{288}f_{3/2} + \frac{335}{192}f_{5/2} + \frac{125}{288}f_{7/2} + \frac{1375}{1152}f_{9/2}\right). \tag{B.3}$$

If we have more than three (five) points we need to stitch the formulas together. We do this by integrating from x_k to x_{k+1}. For the fourth-order stencil we get

$$\int_{x_k}^{x_{k+1}} f(x)\mathrm{d}x \approx \Delta x\left(\frac{1}{24}f_{k-1/2} + \frac{11}{12}f_{k+1/2} + \frac{1}{24}f_{k+3/2}\right) \tag{B.4}$$

and for the sixth-order stencil we get

$$\begin{aligned}\int_{x_k}^{x_{k+1}} f(x)\mathrm{d}x \approx \Delta x\Bigg(&\frac{-17}{5760}f_{k-3/2} + \frac{308}{5760}f_{k-1/2} + \frac{5178}{5760}f_{k+1/2} \\ &+ \frac{308}{5760}f_{k+3/2} - \frac{17}{5760}f_{k+5/2}\Bigg).\end{aligned} \tag{B.5}$$

We present the weights for a fourth-order approximation to the integral in table B1 and for a sixth-order approximation to the integral in table B2. The weights are obtained by using (B.2) and (B.3) at the boundaries and (B.4) and (B.5) on the interior. The stencils are symmetric about the center and so only half the coefficients are shown.

ORCID iDs

Nils Deppe https://orcid.org/0000-0003-4557-4115
François Hébert https://orcid.org/0000-0001-9009-6955
Lawrence E Kidder https://orcid.org/0000-0001-5392-7342
Saul A Teukolsky https://orcid.org/0000-0001-9765-4526

References

[1] Reed W H and Hill T R 1973 Triangular mesh methods for the neutron transport equation *Technical Report* (New Mexico: Los Alamos Scientific Lab.)
[2] Cockburn B and Shu C-W 1989 TVB Runge–Kutta local projection discontinuous Galerkin finite element method for conservation laws: II. General framework *Math. Comput.* **52** 411–35
[3] Cockburn B, Lin S-Y and Shu C-W 1989 TVB Runge–Kutta local projection discontinuous Galerkin finite element method for conservation laws: III. One-dimensional systems *J. Comput. Phys.* **84** 90–113
[4] Cockburn B, Hou S and Shu C-W 990 The Runge–Kutta local projection discontinuous Galerkin finite element method for conservation laws: IV. The multidimensional case *Math. Comput.* **54** 545–81

[5] Jiang G S and Shu C-W 1994 On a cell entropy inequality for discontinuous Galerkin methods *Math. Comp.* **62** 531–8

[6] Barth T, Charrier P and Mansour N N 2001 Energy stable flux formulas for the discontinuous Galerkin discretization of first order nonlinear conservation laws *Technical Report 20010095444* (NASA Technical Reports Server)

[7] Hou S and Liu X-D 2007 Solutions of multi-dimensional hyperbolic systems of conservation laws by square entropy condition satisfying discontinuous Galerkin method *J. Sci. Comput.* **31** 127–51

[8] Godunov S K 1959 A difference method for numerical calculation of discontinuous solutions of the equations of hydrodynamics *Mat. Sb. N.S.* **47** 271–306

[9] Costa B and Don W S 2007 Multi-domain hybrid spectral-WENO methods for hyperbolic conservation laws *J. Comput. Phys.* **224** 970–91

[10] Huerta A, Casoni E and Peraire J 2012 A simple shock-capturing technique for high-order discontinuous Galerkin methods *Int. J. Numer. Methods Fluids* **69** 1614–32

[11] Sonntag M and Munz C-D 2014 Shock capturing for discontinuous Galerkin methods using finite volume subcells *Finite Volumes for Complex Applications VII-Elliptic, Parabolic and Hyperbolic Problems* ed J Fuhrmann, M Ohlberger and C Rohde (Berlin: Springer) pp 945–53

[12] Dumbser M, Zanotti O, Loubère R and Diot S 2014 *A posteriori* subcell limiting of the discontinuous Galerkin finite element method for hyperbolic conservation laws *J. Comput. Phys.* **278** 47–75

[13] Walter B and Dumbser M 2017 Arbitrary-Lagrangian–Eulerian discontinuous Galerkin schemes with *a posteriori* subcell finite volume limiting on moving unstructured meshes *J. Comput. Phys.* **346** 449–79

[14] Zanotti O, Fambri F and Dumbser M 2015 Solving the relativistic magnetohydrodynamics equations with ADER discontinuous Galerkin methods, *a posteriori* subcell limiting and adaptive mesh refinement *Mon. Not. R. Astron. Soc.* **452** 3010–29

[15] Fambri F, Dumbser M, Köppel S, Rezzolla L and Zanotti O 2018 ADER discontinuous Galerkin schemes for general-relativistic ideal magnetohydrodynamics *Mon. Not. R. Astron. Soc.* **477** 4543–64

[16] Núñez-de la Rosa J and Munz C-D 2018 Hybrid DG/FV schemes for magnetohydrodynamics and relativistic hydrodynamics *Comput. Phys. Commun.* **222** 113–35

[17] Boyle M *et al* 2019 The SXS collaboration catalog of binary black hole simulations *Class. Quantum Grav.* **36** 195006

[18] https://black-holes.org/SpEC.html

[19] Scheel M A, Boyle M, Chu T, Kidder L E, Matthews K D and Pfeiffer H P 2009 High-accuracy waveforms for binary black hole inspiral, merger, and ringdown *Phys. Rev.* D **79** 024003

[20] Szilágyi B, Lindblom L and Scheel M A 2009 Simulations of binary black hole mergers using spectral methods *Phys. Rev.* D **80** 124010

[21] Lovelace G, Scheel M A and Szilagyi B 2011 Simulating merging binary black holes with nearly extremal spins *Phys. Rev.* D **83** 024010

[22] Buchman L T, Pfeiffer H P, Scheel M A and Szilagyi B 2012 Simulations of non-equal mass black hole binaries with spectral methods *Phys. Rev.* D **86** 084033

[23] Hemberger D A, Scheel M A, Kidder L E, Szilágyi B, Lovelace G, Taylor N W and Teukolsky S A 2013 Dynamical excision boundaries in spectral evolutions of binary black hole spacetimes *Class. Quantum Grav.* **30** 115001

[24] Scheel M A, Giesler M, Hemberger D A, Lovelace G, Kuper K, Boyle M, Szilágyi B and Kidder L E 2015 Improved methods for simulating nearly extremal binary black holes *Class. Quantum Grav.* **32** 105009

[25] Szilágyi B 2014 Key elements of robustness in binary black hole evolutions using spectral methods *Int. J. Mod. Phys.* D **23** 1430014

[26] Bonazzola S, Gourgoulhon E and Marck J-A 1999 Spectral methods in general relativistic astrophysics *J. Comput. Appl. Math.* **109** 433

[27] Meringolo C and Servidio S 2021 Aliasing instabilities in the numerical evolution of the Einstein field equations *Gen. Relativ. Gravit.* **53** 95

[28] Hilditch D, Weyhausen A and Brügmann B 2016 Pseudospectral method for gravitational wave collapse *Phys. Rev.* D **93** 063006

[29] Rashti A, Fabbri F M, Brügmann B, Chaurasia S V, Dietrich T, Ujevic M and Tichy W 2022 New pseudospectral code for the construction of initial data *Phys. Rev.* D **105** 104027

[30] Meringolo C, Servidio S and Veltri P 2021 A spectral method algorithm for numerical simulations of gravitational fields *Class. Quantum Grav.* **38** 075027

[31] Tichy W 2009 Long term black hole evolution with the BSSN system by pseudospectral methods *Phys. Rev.* D **80** 104034
[32] Kidder L E *et al* 2017 SpECTRE: a task-based discontinuous Galerkin code for relativistic astrophysics *J. Comput. Phys.* **335** 84–114
[33] Deppe N *et al* 2022 *SpECTRE v2022.04.04*
[34] Baumgarte T W and Shapiro S L 2010 *Numerical Relativity: Solving Einstein's Equations on the Computer* (Cambridge: Cambridge University Press)
[35] Rezzolla L and Zanotti O 2013 *Relativistic Hydrodynamics* (Oxford: Oxford University Press)
[36] Antón L, Zanotti O, Miralles J A, Martí J M, Ibáñez J M, Font J A and Pons J A 2006 Numerical 3 + 1 general relativistic magnetohydrodynamics: a local characteristic approach *Astrophys. J.* **637** 296–312
[37] Font J A 2008 Numerical hydrodynamics and magnetohydrodynamics in general relativity *Living Rev. Relativ.* **11** 7
[38] Misner C W, Thorne K S and Wheeler J A 1973 *Gravitation* (San Francisco, CA: Freeman)
[39] Dedner A, Kemm F, Kröner D, Munz C-D, Schnitzer T and Wesenberg M 2002 Hyperbolic divergence cleaning for the MHD equations *J. Comput. Phys.* **175** 645–73
[40] Mösta P *et al* 2014 GRHydro: a new open-source general-relativistic magnetohydrodynamics code for the Einstein toolkit *Class. Quantum Grav.* **31** 015005
[41] Teukolsky S A 2016 Formulation of discontinuous Galerkin methods for relativistic astrophysics *J. Comput. Phys.* **312** 333–56
[42] Hesthaven J S and Warburton T 2008 *Nodal Discontinuous Galerkin Methods: Algorithms, Analysis, and Applications* (Berlin: Springer)
[43] Scheel M A, Pfeiffer H P, Lindblom L, Kidder L E, Rinne O and Teukolsky S A 2006 Solving Einstein's equations with dual coordinate frames *Phys. Rev.* D **74** 104006
[44] Dumbser M, Castro M, Parés C and Toro E F 2009 ADER schemes on unstructured meshes for nonconservative hyperbolic systems: applications to geophysical flows *Comput. Fluids* **38** 1731–48
[45] Dal Maso G, LeFloch P G and Murat F 1995 Definition and weak stability of nonconservative products *J. Math. Pures Appl.* **74** 483–548
[46] Minoli C A A and Kopriva D A 2011 Discontinuous Galerkin spectral element approximations on moving meshes *J. Comput. Phys.* **230** 1876–902
[47] Shu C-W and Osher S 1988 Efficient implementation of essentially non-oscillatory shock-capturing schemes *J. Comput. Phys.* **77** 439–71
[48] Throwe W and Teukolsky S 2020 A high-order, conservative integrator with local time-stepping *SIAM J. Sci. Comput.* **42** A3730–60
[49] Mersman W A 1965 *Self-starting Multistep Methods for the Numerical Integration of Ordinary Differential Equations* (National Aeronautics and Space Administration)
[50] Cockburn B, Karniadakis G E and Shu C-W 2000 The development of discontinuous Galerkin methods *Discontinuous Galerkin Methods* (Berlin: Springer) pp 3–50
[51] Cockburn B and Shu C-W 2001 Runge–Kutta discontinuous Galerkin methods for convection-dominated problems *J. Sci. Comput.* **16** 173–261
[52] Krivodonova L and Qin R 2013 An analysis of the spectrum of the discontinuous Galerkin method *Appl. Numer. Math.* **64** 1–18
[53] Deppe N *et al* Simulating magnetized neutron stars with discontinuous Galerkin methods *Phys. Rev.* D **105** 123031
[54] Cockburn B and Shu C-W 1998 The Runge–Kutta discontinuous Galerkin method for conservation laws: V *J. Comput. Phys.* **141** 199–224
[55] Krivodonova L, Xin J, Remacle J-F, Chevaugeon N and Flaherty J E 2004 Shock detection and limiting with discontinuous Galerkin methods for hyperbolic conservation laws *Appl. Numer. Math.* **48** 323–38
[56] Krivodonova L 2007 Limiters for high-order discontinuous Galerkin methods *J. Comput. Phys.* **226** 879–96
[57] Zhong X and Shu C-W 2013 A simple weighted essentially nonoscillatory limiter for Runge–Kutta discontinuous Galerkin methods *J. Comput. Phys.* **232** 397–415
[58] Zhu J, Zhong X, Shu C-W and Qiu J 2016 Runge–Kutta discontinuous Galerkin method with a simple and compact Hermite WENO limiter *Commun. Comput. Phys.* **19** 944–69
[59] Wang C, Zhang X, Shu C-W and Ning J 2012 Robust high order discontinuous Galerkin schemes for two-dimensional gaseous detonations *J. Comput. Phys.* **231** 653–65

[60] Maday Y, Mavriplis C and Patera A T 1989 Nonconforming mortar element methods—application to spectral discretizations *Domain Decomposition Methods* (NASA Langley Research Center: Hampton) pp 392–418
[61] Kopriva D A 1996 A conservative staggered-grid Chebyshev multidomain method for compressible flows: II. A semi-structured method *J. Comput. Phys.* **128** 475–88
[62] Kopriva D A, Woodruff S L and Hussaini M Y 2002 Computation of electromagnetic scattering with a non-conforming discontinuous spectral element method *Int. J. Numer. Methods Eng.* **53** 105–22
[63] Bui-Thanh T and Ghattas O 2012 Analysis of an *hp*-nonconforming discontinuous Galerkin spectral element method for wave propagation *SIAM J. Numer. Anal.* **50** 1801–26
[64] Persson P-O and Peraire J 2006 Sub-cell shock capturing for discontinuous Galerkin methods *44th AIAA Aerospace Sciences Meeting and Exhibit* (American Institute of Aeronautics and Astronautics, Inc.)
[65] Gottlieb D and Orszag S A 1977 *Numerical Analysis of Spectral Methods* (Society for Industrial and Applied Mathematics)
[66] Dormand J R and Prince P J 1980 A family of embedded Runge–kutta formulae *J. Comput. Appl. Math.* **6** 19–26
[67] Balsara D 2001 Total variation diminishing scheme for relativistic magnetohydrodynamics *Astrophys. J. Suppl.* S **132** 83–101
[68] Giacomazzo B and Rezzolla L 2006 The exact solution of the Riemann problem in relativistic magnetohydrodynamics *J. Fluid Mech.* **562** 223–59
[69] Leismann T, Antón L, Aloy M A, Müller E, Martí J M, Miralles J A and Ibáñez J M 2005 Relativistic MHD simulations of extragalactic jets *Astron. Astrophys.* **436** 503–26
[70] Del Zanna L, Zanotti O, Bucciantini N and Londrillo P 2007 ECHO: a Eulerian conservative high-order scheme for general relativistic magnetohydrodynamics and magnetodynamics *Astron. Astrophys.* **473** 11–30
[71] Balsara D S and Spicer D S 1999 A staggered mesh algorithm using high order Godunov fluxes to ensure solenoidal magnetic fields in magnetohydrodynamic simulations *J. Comput. Phys.* **149** 270–92
[72] Tóth G 2000 The $\nabla B = 0$ constraint in shock-capturing magnetohydrodynamics codes *J. Comput. Phys.* **161** 605–52
[73] Etienne Z B, Liu Y T and Shapiro S L 2010 Relativistic magnetohydrodynamics in dynamical spacetimes: a new adaptive mesh refinement implementation *Phys. Rev.* D **82** 084031
[74] Del Zanna L, Bucciantini N and Londrillo P 2003 An efficient shock-capturing central-type scheme for multidimensional relativistic flows *Astron. Astrophys.* **400** 397–413
[75] DeVore C R 1991 Flux-corrected transport techniques for multidimensional compressible magnetohydrodynamics *J. Comput. Phys.* **92** 142–60
[76] Beckwith K and Stone J M 2011 A second-order Godunov method for multi-dimensional relativistic magnetohydrodynamics *Astrophys. J. Suppl.* **193** 6
[77] Gardiner T A and Stone J M 2005 An unsplit Godunov method for ideal MHD via constrained transport *J. Comput. Phys.* **205** 509–39
[78] Stone J M, Gardiner T A, Teuben P, Hawley J F and Simon J B 2008 Athena: a new code for astrophysical MHD *Astrophys. J. Suppl.* S **178** 137–77
[79] Tolman R C 1939 Static solutions of Einstein's field equations for spheres of fluid *Phys. Rev.* **55** 364–73
[80] Oppenheimer J R and Volkoff G M 1939 On massive neutron cores *Phys. Rev.* **55** 374–81
[81] Cipolletta F, Kalinani J V, Giacomazzo B and Ciolfi R 2020 Spritz: a new fully general-relativistic magnetohydrodynamic code *Class. Quantum Grav.* **37** 135010
[82] Font J A, Goodale T, Iyer S, Miller M, Rezzolla L, Seidel E, Stergioulas N, Suen W-M and Tobias M 2002 Three-dimensional numerical general relativistic hydrodynamics: II. Long-term dynamics of single relativistic stars *Phys. Rev.* D **65** 084024
[83] Cook G B, Shapiro S L and Teukolsky S A 1992 Spin-up of a rapidly rotating star by angular momentum loss—effects of general relativity *Astrophys. J.* **398** 203
[84] Cook G B, Shapiro S L and Teukolsky S A 1994 Rapidly rotating neutron stars in general relativity: realistic equations of state *Astrophys. J.* **424** 823
[85] Hunter J D *et al* 2007 Matplotlib: A 2D graphics environment *Computing in Science Engineering* **9** 90–5
[86] Hunter J D 2007 Matplotlib: a 2D graphics environment *Comput. Sci. Eng.* **9** 90–5

[87] Caswell T A *et al* 2020 *Matplotlib/Matplotlib: Rel: v3.3.0*
[88] Tantau T 2021 *The Tikz and Pgf Packages*
[89] Ayachit U 2015 *The ParaView Guide: A Parallel Visualization Application* (Clifton Park, NY: Kitware, Inc.)
[90] Ahrens J, Geveci B and Law C 2005 Paraview: an end-user tool for large-data visualization *The Visualization Handbook*
[91] Sebastian K and Shu C-W 2003 Multidomain WENO finite difference method with interpolation at subdomain interfaces *J. Sci. Comput.* **19** 405–38
[92] Wolf W R and Azevedo J L F 2007 High-order ENO and WENO schemes for unstructured grids *Int. J. Numer. Methods Fluids* **55** 917–43
[93] Tsoutsanis P, Antoniadis A F and Drikakis D 2014 WENO schemes on arbitrary unstructured meshes for laminar, transitional and turbulent flows *J. Comput. Phys.* **256** 254–76
[94] Tsoutsanis P 2019 Stencil selection algorithms for WENO schemes on unstructured meshes *J. Comput. Phys.* X **4** 100037
[95] Farmakis P S, Tsoutsanis P and Nogueira X 2020 WENO schemes on unstructured meshes using a relaxed *a posteriori* MOOD limiting approach *Comput. Methods Appl. Mech. Eng.* **363** 112921
[96] Dumbser M, Käser M, Titarev V A and Toro E F 2007 Quadrature-free non-oscillatory finite volume schemes on unstructured meshes for nonlinear hyperbolic systems *J. Comput. Phys.* **226** 204–43
[97] Sheng C, Zhao Q, Zhong D and Ning G 2019 A strategy to implement high-order WENO schemes on unstructured grids *AIAA Aviation 2019 Forum* (American Institute of Aeronautics and Astronautics, Inc.)
[98] Freret L, Ivan L, De Sterck H and Groth C P 2017 A high-order finite-volume method with anisotropic AMR for ideal MHD flows *55th AIAA Aerospace Sciences Meeting* (American Institute of Aeronautics and Astronautics, Inc.)